ADVANCED MATERIALS INTERFACES
Open Access
www.advmatinterfaces.de

Preparation and Characterization of $GdVO_4$:Tb,Eu Nanoparticles/ Carbon Dots Composites via Hydrothermal Deposition and Physical Mixing for Luminescent Nanothermometry

*Rut Sisó-Moliné, Concepción Cascales, Maria Méndez, Laura Fuentes-Rodriguez, Araceli de Aquino, Maria Cinta Pujol, Carlos Zaldo, and Joan J. Carvajal**

Carbon dots (CDs) stand out for their facile synthesis, strong photoluminescence, and easy surface modification, making them excellent candidates for integration with other nanostructures to enhance physical and chemical properties.In this work, CDs derived from eco-friendly precursors (xylose and biomass-derived hemicellulose) are combined with $GdVO_4$:Tb,Eu nanoparticles (NPs) via two distinct approaches: (i) hydrothermal deposition onto the lanthanide-doped particles and (ii) physical mixing of prefabricated components. Notably, the spectroscopic properties of the resulting composites depend on the fabrication route. While method (i) enables competitive energy transfers from the vanadate charge transfer band (CTB) to Eu^{3+} and CDs, method (ii), which involves lower concentrations of the emissive components, promotes a cooperative mechanism wherein CDs sensitize the CTB, enhancing the Eu^{3+} red emission. In both scenarios, Tb^{3+} is believed to serve as an intermediary, aiding the repopulation of the Eu^{3+} ^5D_j energy levels. The dual-emissive nature of the composites results in violet-magenta chromaticity, reflecting intermediate behavior between the blue CDs and red-emitting Ln-NPs, and supporting their use in tunable optical applications. The described mechanisms also influence the composites' performance as ratiometric nanothermometers. Upon evaluating their thermal response from 298 K to 358 K, distinct behaviors emerge, with relative thermal sensitivities ranging from 0.84% K^{-1} (298 K) to 5.6% K^{-1} (358 K)—the latter being among the highest reported for similar materials.

1. Introduction

Since their discovery in 2004 by Xu et al.,[1] carbon dots (CDs) have garnered considerable attention due to their unique properties and ease of fabrication. CDs stand out for their simple, sustainable, and cost-effective manufacturing processes,[2,3] as well as their tunable luminescent and surface properties,[4] high photostability, low toxicity, and excellent biocompatibility. These characteristics make CDs promising candidates for a wide variety of applications, including optoelectronic devices,[5] bioimaging,[6,7] anticounterfeiting systems,[8,9] luminescent sensing,[10–12] and more.

A key advantage of CDs lies in their facile and versatile synthesis methods, which allow for straightforward surface chemistry modifications and nanoscale integration. This adaptability facilitates their combination with other materials to form composites with enhanced or novel physico-chemical properties. Among the most commonly used counterparts in such composites are trivalent

R. Sisó-Moliné, L. Fuentes-Rodriguez, M. C. Pujol, J. J. Carvajal
Departament de Química Física i Inorgànica, Photonic (nano)materials and techniques for optical sensing (PhO2TO)
Universitat Rovira i Virgili
Marcel·lí Domingo, 1, Tarragona 43007, Spain
E-mail: joanjosep.carvajal@urv.cat

The ORCID identification number(s) for the author(s) of this article can be found under https://doi.org/10.1002/admi.202500410

DOI: 10.1002/admi.202500410

C. Cascales, C. Zaldo
Concepción Cascales, Carlos Zaldo, Instituto de Ciencia de Materiales de Madrid
c/Sor Juana Inés de la Cruz
Cantoblanco, Madrid 28049, Spain

M. Méndez
Institut Català d'investigació Química (ICIQ)
The Barcelona Institute of Science and Technology (BIST)
Avda. Països Catalans, 16, Tarragona 43007, Spain

A. de Aquino
Araceli de Aquino, Universitat de Barcelona, Supra and Nanostructured Systems Research Group
Inorganic Chemistry Section, Faculty of Chemistry
Martí i Franques 1–11, Barcelona 08028, Spain

lanthanide (Ln)-doped phosphors.[13–17] These materials consist of a dielectric host matrix doped with optically active Ln^{3+} ions. They exhibit narrow spectral bands, large Stokes shifts, and long decay times,[18] making them attractive for applications requiring precise luminescent performance. However, these materials present some intrinsic limitations, including low absorption cross-sections (i. e., poor photoexcitation efficiency of f-f transitions), and low luminescence intensity due to parity selection rules.[19]

The incorporation of CDs as sensitizers has proven to be an effective strategy to overcome these limitations. CDs offer broad absorption spectra and efficient energy transfer capabilities, enhancing the optical performance of Ln^{3+}-doped materials when combined with them.[13,20,21]

In addition to improving luminescence intensity, the impregnation with CDs introduces an organic-like emissive center that markedly differs from Ln^{3+} ions in both structure and photoluminescence mechanisms. These differences result in distinct sensitivities to specific parameters, such as analyte concentration[22–24] or temperature.[13–17] The coexistence of these differential responses to a single stimulus enables the development of sensing strategies more robust than the typical single-band (SB) luminescent thermometric approach, which only takes into account a particular emission peak at a specific excitation wavelength. Ratiometric schemes, in contrast, compare two emission signals, so that the sensor itself functions as a self-referenced system, mitigating the influence of environmental factors, power fluctuation or illumination oscillations of the excitation source, the signal-to-noise ratio and instabilities in the detection set-up system, the absorption and scatter cross-sections of the emitters, the variation of the concentration of emitters in the sample where the temperature is going to be measured, or the inhomogeneity on the distribution of the emitters in the luminescent thermal probes.[25]

Given the increasing demand for precise temperature management and monitoring in fields such as biomedical diagnostics,[26] nanotechnology, and energy systems,[27] the development of highly sensitive and reliable nanothermometers has become a priority. Ln-nanoparticles (NPs)/CD composites have recently emerged as possible candidates to tackle this need, but the field is still in its early stages. Only a few articles have been published addressing this specific topic and all of them have in common the use of the Eu^{3+} ion as the lanthanide counterpart (taking advantage of its $^5D_0 \rightarrow {}^7F_1$, $^5D_0 \rightarrow {}^7F_2$, and/or $^5D_0 \rightarrow {}^7F_0$ electronic transitions that lead to a red emission) and the selection of blue-green emitting CDs as sensitizers.[13–17] On the contrary, the host materials are diverse, including metalorganic frameworks (MOFs),[14,15] perovskites,[13,17] or vanadates,[16] and the evaluated temperature ranges span from room temperature up to a maximum of 480 K.

To gain insight into the subject, in this work we present a comprehensive study on the synthesis of $GdVO_4$:Tb,Eu/CD composites, exploring different methodologies and carbon sources. We further investigate their physical and spectroscopic characteristics, revealing that the fabrication route critically influences their photoluminescent behavior, with CDs either competing with or sensitizing Eu^{3+} emission. The performance of all synthesized materials as ratiometric luminescent thermometric sensors was also evaluated. Notably, the best-performing composite achieved a maximum relative thermal sensitivity of 5.6% K^{-1}; at 358 K, underscoring the strong potential of these materials for advanced luminescent thermometry applications.

2. Preparation Methods

The composites analyzed in this study consist of CDs combined with $GdVO_4$ nanoparticles doped with lanthanides (Ln-NPs), specifically 15 at. % Tb and either 2 at. % or 5 at. % Eu (denoted as Ln-NP-2Eu and Ln-NP-5Eu, respectively) substituting Gd in the structures. These concentrations of lanthanide ions were chosen according to recent studies that indicates that they are in the optimum range for several similar materials used as luminescent thermometers.[28] These nanoparticles were synthesized via a hydrothermal method followed by a calcination step to enhance their luminescent emission efficiency.[29]

Table 1 summarizes the synthesis conditions of each sample, with further details provided in the Experimental Section. Briefly, the temperature needed in the hydrothermal reaction was achieved by two different heating methods: microwave-assisted hydrothermal synthesis (MW) and conventional hydrothermal treatment in a convection oven (HTC). For each method, CDs were synthesized through a hydrothermal process, while composites were prepared using either hydrothermal deposition (D)—where Ln-NPs were incorporated directly into the CD precursor solution, allowing simultaneous synthesis of both CDs and composites—or physical mixing (M), in which pre-synthesized CDs and Ln-NPs were combined under stirring.

To reinforce the sustainability of our approach, we explored two different carbon precursors for CDs preparation. First, commercial xylose (X) was used as a model compound. Subsequently, we replaced it with a bio-based carbon feedstock—hemicellulose extracted from crushed almond shells (H)—as it is primarily composed of xylose.

The selection of Ln-NP type (Ln-NP-5Eu or Ln-NP-2Eu) and concentration was carefully optimized to ensure that the Eu^{3+} emission intensity was comparable to that of the CDs, thereby enabling reliable evaluation of the composites' ratiometric thermometric performance. Since the CD emission was more intense in the D-composites than in the M-composites, a higher concentration of Ln-NP (2.50 mg mL^{-1} of Ln-NP-5Eu) was used for the former, whereas a lower concentration (0.25 mg mL^{-1} of Ln-NP) was used for the latter. Specifically, Ln-NP-5Eu was used for X-derived composites, while Ln-NP-2Eu was selected for H-derived composites to further balance the relative emission intensities of CDs and Eu^{3+}. This adjustment was necessary because the H-derived CDs exhibit lower luminescence intensity than their X-derived counterparts.

All samples were purified. CDs were initially separated from high-molecular-weight byproducts through filtration, followed by the removal of low-molecular-weight fluorophores via dialysis. The purified CD solutions were either directly analyzed or mixed with Ln-NPs to prepare the M-composites. In the case of D-composites, the products were collected as solids by filtration and then redispersed in fresh deionized (DI) water. An exception was observed for the Comp-HTC-X-D sample, where the synthesis conditions resulted in the formation of large amounts of solid coke mixed with the desired product, quenching its emission (Figure S1, Supporting Information). Due to the inability to

Table 1. Summary of the CDs and $GdVO_4$:Tb,Eu nanoparticles / CDs composites prepared. Sample nomenclature is based on the synthesis conditions. The concentration of lanthanide-doped nanoparticles used in each composite are specified in footnotes. Abbreviations: CD – Carbon Dot, Comp – Composite, MW – Microwave-Assisted Hydrothermal, HTC – Conventional Hydrothermal, X – Commercial Xylose, H – Extracted Hemicellulose, D – Hydrothermal Deposition, M – Physical Mixing.

	Microwave oven				Conventional convection oven			
	CD	Composites			CD	Composites		
	Hydrothermal Synthesis	Hydrothermal Deposition		Physical Mixing	Hydrothermal Synthesis	Hydrothermal deposition		Physical Mixing
Commercial Xylose	CD-MW-X	Comp-MW-X-D[a)]		Comp-MW-X-M[b)]	CD-HTC-X	Comp-HTC-X-D[c)]		Comp-HTC-X-M[b)]
Extracted Hemicellulose	CD-MW-H	Comp-MW-H-D[a)]		Comp-MW-H-M[d)]	CD-HTC-H	Comp-HTC-H-D[a)]		Comp-HTC-H-M[d)]

[a)] 2.50 mg mL^{-1} of Ln-NP-5Eu; [b)] 0.25 mg mL^{-1} of Ln-NP-5Eu; [c)] Experimentally impossible to separate composites from by-products. The sample was then excluded from the study; [d)] 0.25 mg mL^{-1} of Ln-NP-2Eu.

separate these phases by either filtration or centrifugation, this sample was excluded from the study.

Scheme 1 summarizes the experimental flow chart for the preparation of the composites.

3. Characterization

3.1. Structure, Morphology and Composition

The morphology of composites and their individual constitutional elements was studied by electron microscopy techniques, including Transmission Electron Microscopy (TEM) and Field-Emission Scanning Electron Microscopy (FESEM). **Figures 1** and **2** show the characterization of the individual elements.

As can be seen in Figure 1a, the dry Ln-NP obtained after hydrothermal synthesis present prismoid shapes with the longitudinal dimension being around 40 nm and the transversal dimension of less than 20 nm. Nevertheless, once the Ln-NPs were exposed to calcination at 900 °C, they agglomerated and led to ellipsoidal structures with dimensions bigger than 100 nm (Figure 1b. As depicted in Figure 1c, the X-Ray Diffraction (XRD) pattern recorded for the Ln-NPs agreed with that of a pure tetragonal $GdVO_4$ crystalline structure (PDF # 17–0260), with the most intense diffraction peaks being the ones located at 2θ = 24.7°, 33.3°, 49.2°, and 18.6°, corresponding to crystallographic planes (200), (112), (312), and (101), respectively. Fourier-Transformed Infrared (FTIR) spectroscopy also confirmed the composition of Ln-NP, showing a wide intense band centered at 749 cm^{-1} and a narrower one positioned at 445 cm^{-1} that correspond, respectively, to the V—O and Gd—O stretching vibrations. The absence of a broad band at 3310 cm^{-1} (H—O—H vibrations) confirms the effectivity of the calcination process to remove hydration (Figure 1d).[29]

Regarding CDs (**Figure 2**), all samples exhibit quasi-spherical morphologies, and their amorphous nature was confirmed by electron diffraction, as no diffraction patterns were observed. A key observation is the difference in sizes depending on the fabrication method: CDs synthesized from commercial xylose (Figure 2a and b) are substantially larger (52 ± 20 nm – CD-MW-X, and 41 ± 5 nm – CD-HTC-X) than those prepared from extracted hemicellulose (1.7 ± 0.4 nm – CD-HTC-H). The size distribution of the CDs was calculated based on the analysis of the TEM images, and the mean diameters correspond to those of at least 60 individual carbon dots (CDs) for each kind, measured from multiple TEM images acquired from different regions of the samples. These sizes distributions can be seen in Figure S2 in the Supporting Information. Notice that in the case of CD-MW-H (Figure 2d), the CDs could not be detected by TEM, probably because of their low concentration and small size. Nevertheless, their presence was confirmed by spectroscopic analysis, as discussed in Section 3.2.1.

The aforementioned differences in sizes may be attributed to the composition of the hemicellulose used in the synthesis process, which, although primarily composed of xylose (and xylan, its polymerized form), also contains minor amounts of other monosaccharides and their respective polymerization products (mainly glucose and arabinose, and smaller proportions of rhamnose and galactose).[30–32] Furthermore, the acidic hydrothermal treatment applied to the almond shell precursor (see

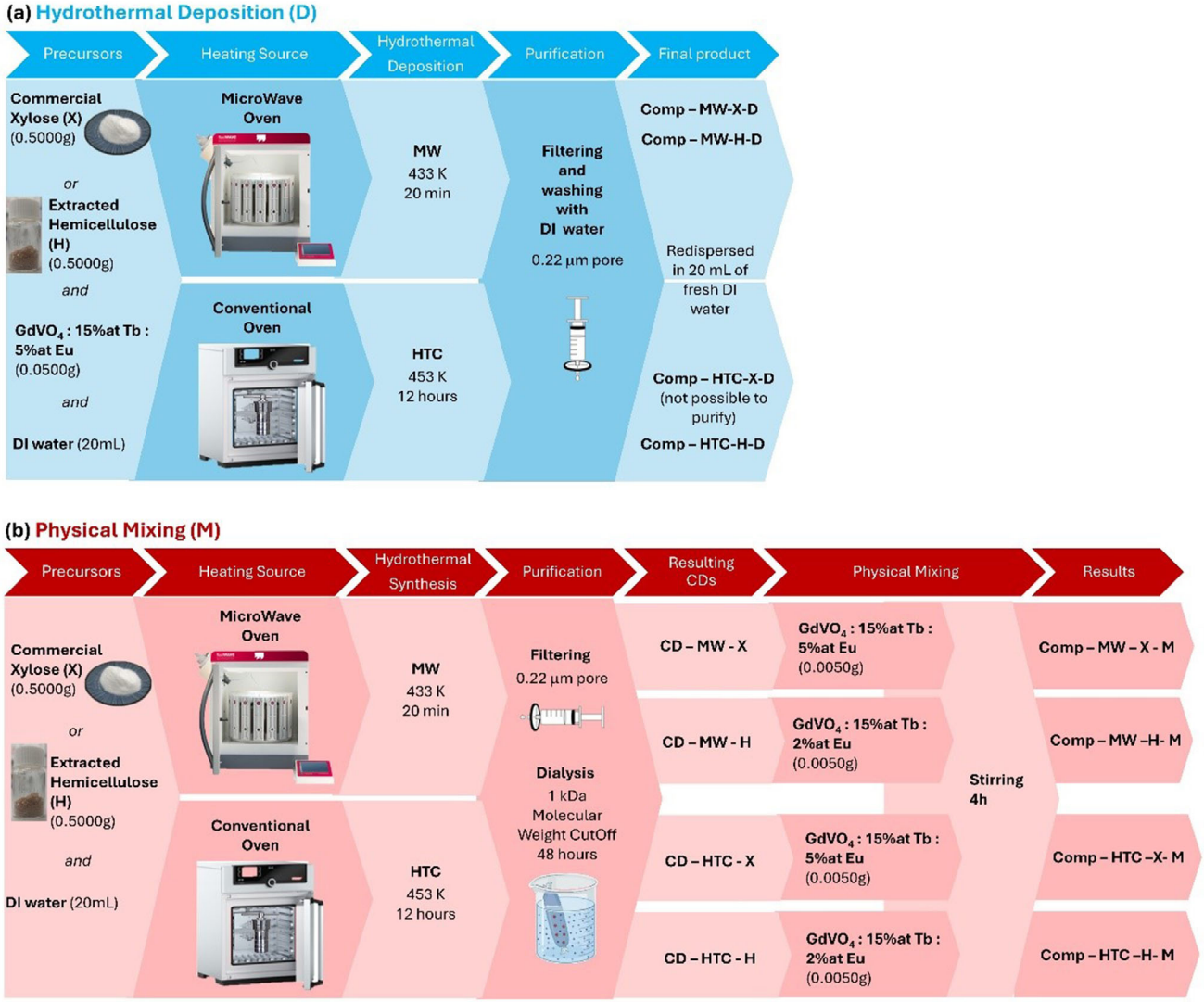

Scheme 1. Experimental flowchart of the preparation procedure for the different composites prepared in the paper. DI water: Deionized water; MW: MicroWave; HTC: Conventional Hydrothermal Carbonization.

Experimental Section) results in the formation of degradation byproducts due to monosaccharide dehydration, leading to the generation of furfural derivatives and low molecular weight acids such as formic and acetic acid.[30,31] In our specific case, the main constituents of the hemicellulosic precursor were xylose (76%) and acetic acid (20%) while smaller percentages of glucose, furfural, and hydroxymethylfurfural were detected via High-Performance Liquid Chromatography (HPLC) (Table S1, Supporting Information). The presence of these additional chemical species might introduce changes in the CDs formation mechanisms. As widely documented, xylose readily degrades into furfural under thermal processing.[33–36] Subsequently, as reported by Almohofer et al.,[37] furfural degradation can follow two different pathways: an acid-catalyzed degradation to formic acid and C_4 species, and an uncatalyzed direct polymerization pathway. We hypothesize that the acidic conditions of the hemicellulose precursor solution (pH = 5) enhance nucleation by catalyzing xylose dehydration into furfural and the subsequent degradation to formic acid and C_4 species. In contrast, the neutral conditions provided by commercial xylose favored the uncatalyzed polymerization route, ultimately resulting in larger nanoparticles (Figure 2e).

The size differences of CDs, along with the composite preparation methodology, significantly influence the final composite configuration (Figure 3a–g). As observed in Figure 3d and f, composites synthesized by physical mixing of commercial xylose – derived CDs with 0.25 mg mL^{-1} of Ln-NP-5Eu (i. e., Comp-MW-X-M and Comp-HTC-X-M), clearly exhibit carbon nanoparticles (appearing in lighter color in the image due to the low atomic weight of carbon, and some of them highlighted with dashed circles) attached to the Ln-NP (which appear more contrasted owing to their heavier elemental composition). In contrast, for composites prepared using the same method but incorporating 0.25 mg mL^{-1} of Ln-NP-2Eu and hemicellulose as CDs

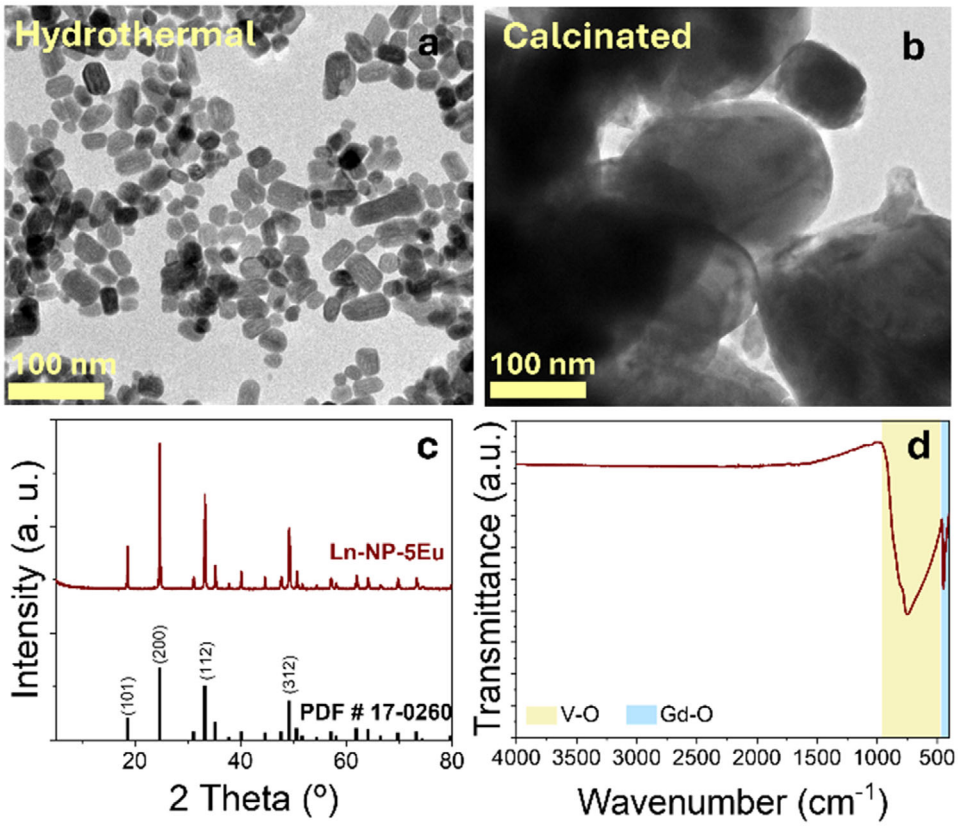

Figure 1. Characterization of Ln-NP. a) TEM image of hydrothermally synthesized Ln-NPs and b) TEM image of Ln-NPs after calcination at 900 °C. c) XRD pattern showing the structural analysis of the samples, with the reference PDF for tetragonal $GdVO_4$ (black) included for comparison. d) FTIR spectra of the Ln-NP. The shaded yellow and blue regions correspond to v_s(V–O) and v_s(Gd/Ln–O) vibrational modes, respectively.

precursor (Comp-MW-H-M and Comp-HTC-H-M), the CDs become more challenging to distinguish. As shown in Figure 3e and g, an organic matrix (appearing as a grey cloud indicated by yellow arrows) surrounds the Ln-NP, with only a few embedded CDs (highlighted with dashed circumferences). The primary factor contributing to the difficulty of identifying CDs in these cases is the amplitude contrast inherent to the TEM technique. This contrast (understood as the difference between intensities) arises from incoherent elastic scattering (Rutherford scattering) of electrons, which is a strong function of atomic number Z (hence the mass or the density), and the thickness of the specimen.[38] As a result, the Ln-NP, composed of heavier elements and larger in size compared to the CDs, interact more strongly with the electron beam and appear with significantly higher contrast. Consequently, the higher contrast of the Ln-NP obscures the presence of the CDs, making them less discernible in the TEM images.

Similar issues appeared for samples prepared via hydrothermal deposition (Figures 3a; S3, Supporting Information). TEM images revealed a surface texture with lower contrast compared to the bulk Ln-NP, which could be attributed to the presence of CDs. Additionally, FESEM images (Figures 3b; Figure S3b, Supporting Information) displayed some quasi-spherical protuberances, which were considered indicative of CD attachment.

To further confirm the composition of the samples, Energy Dispersive X-Ray (EDX) spectroscopy was performed. The EDX mapping of Comp-MW-X-D (Figure 3h; Figure S4, Supporting Information) confirmed the presence of Gd, Eu, Tb, V, O, and C, supporting the successful coupling of CDs onto the Ln-NP surface. Further characterization by FTIR spectroscopy (Figure 3i) revealed a spectrum consistent with that of pristine Ln-NP-5Eu, with characteristic bands at 749 cm^{-1} and 445 cm^{-1} corresponding to V—O and Gd—O stretching vibrations, respectively. Notably, no significant absorption bands associated with CDs – such as C═O stretching at ≈1720 cm^{-1} and C═C stretching at ≈1620 cm^{-1} [39–41] – were detected. The absence of these vibration bands could be attributed to the low CD content in relation to Ln-NPs, as previously reported by other authors.[42,43]

XRD analysis of Comp-MW-X-D (Figure 3j) further confirmed the structural integrity of the composite. Given the amorphous nature of CDs observed in TEM, along with their low content and high dispersion, the diffraction pattern predominantly matched that of pristine Ln-NP-5Eu. This finding agrees with previously reported articles[13,42,44,45] and suggests that the tetragonal $GdVO_4$ crystal structure remained unchanged upon CDs incorporation. However, two additional low-intensity peaks (Inset in Figure 3j) were observed at 2θ = 14.1° and 16.8°, with the former potentially indicating the presence of small amounts of graphite oxide derived from precursor carbonization, as suggested by previous studies.[46]

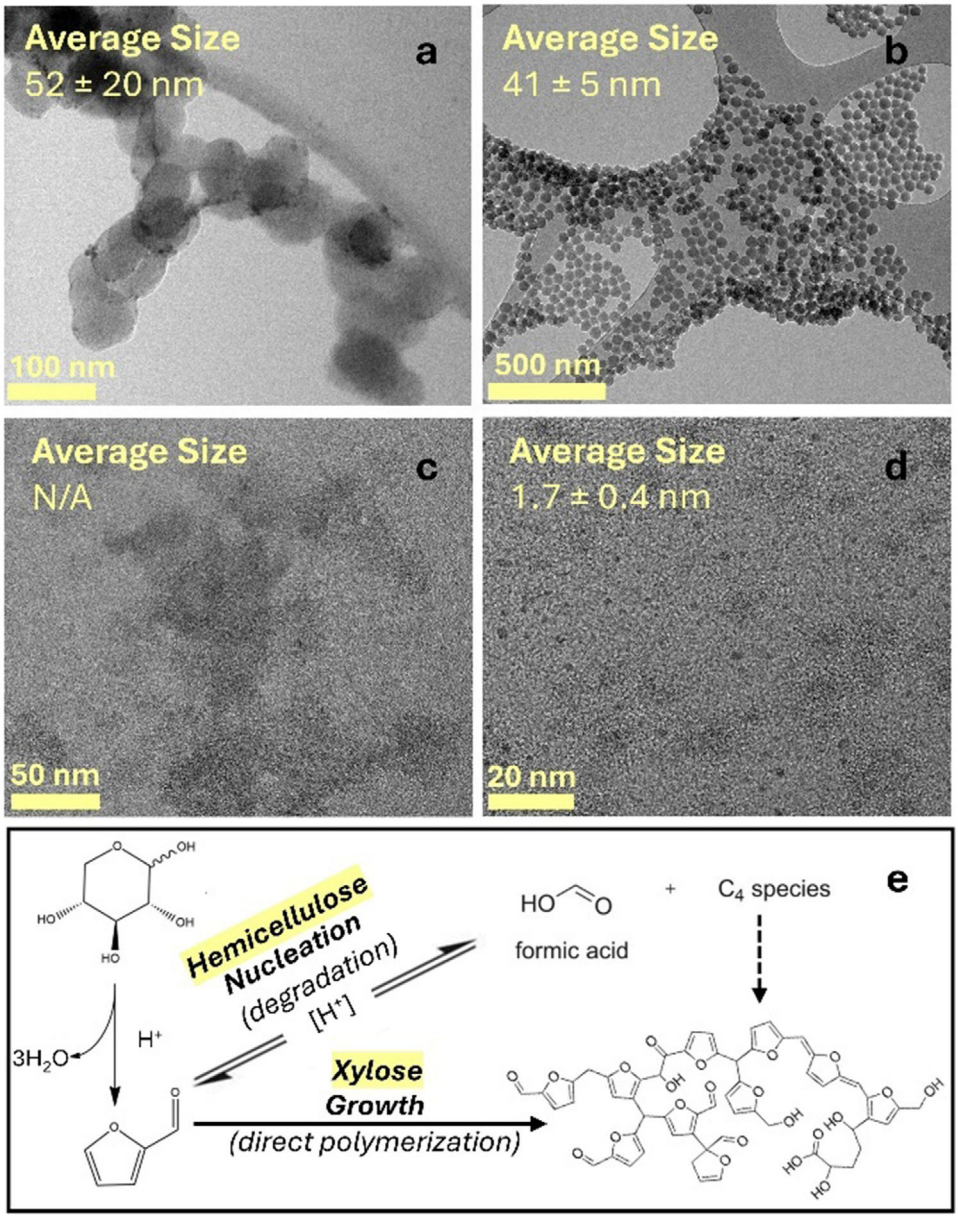

Figure 2. Morphological characterization TEM imaging of a) CD-MW-X and b) CD-HTC-X, showing their respective particle sizes. c) CD-MW-H, where individual nanoparticles could not be distinguished, and d) CD-HTC-H, exhibiting a significantly smaller size distribution. e) Schematic representation of the proposed CDs' formation mechanism, highlighting the role of precursor on the preferred pathway (acid-catalyzed nucleation or uncatalyzed growth). The latter adapted with permission ref. [37].

3.2. Spectroscopic Characteristics

3.2.1. Spectroscopic Properties

To further investigate the formation of the composites, their spectroscopic properties were evaluated, alongside those of their individual components.

For this purpose, photoluminescence (PL) emissions over the 330–500 nm excitation range were analyzed, as shown in **Figure 4**. CDs exhibited the characteristic excitation-wavelength-dependent emission, with maximum intensities in the blue region (≈440–450 nm) under ultraviolet (UV) excitation (≈375 nm) (Figure 4a). In contrast, Ln-NPs primarily exhibited emissions corresponding to ^{5}Do → $^7F_1$and^{5}Do → $^7F_2$ transitions of Eu^{3+} (dominating the profile) and $^5D_4$ → $^7F_5$ transitions of Tb^{3+} (less intense and more perceptible at low Eu^{3+} doping concentrations) upon excitation at 330 nm (Figure 4c). Excitation at wavelengths other than 330 nm did not result in significant emission, except for excitation at 400 nm and 500 nm, which produced peaks at similar positions but with notably lower intensity (inset in Figure 4c). All these behaviors can be understood by the analysis of absorbance and excitation spectra, as we will comment later.

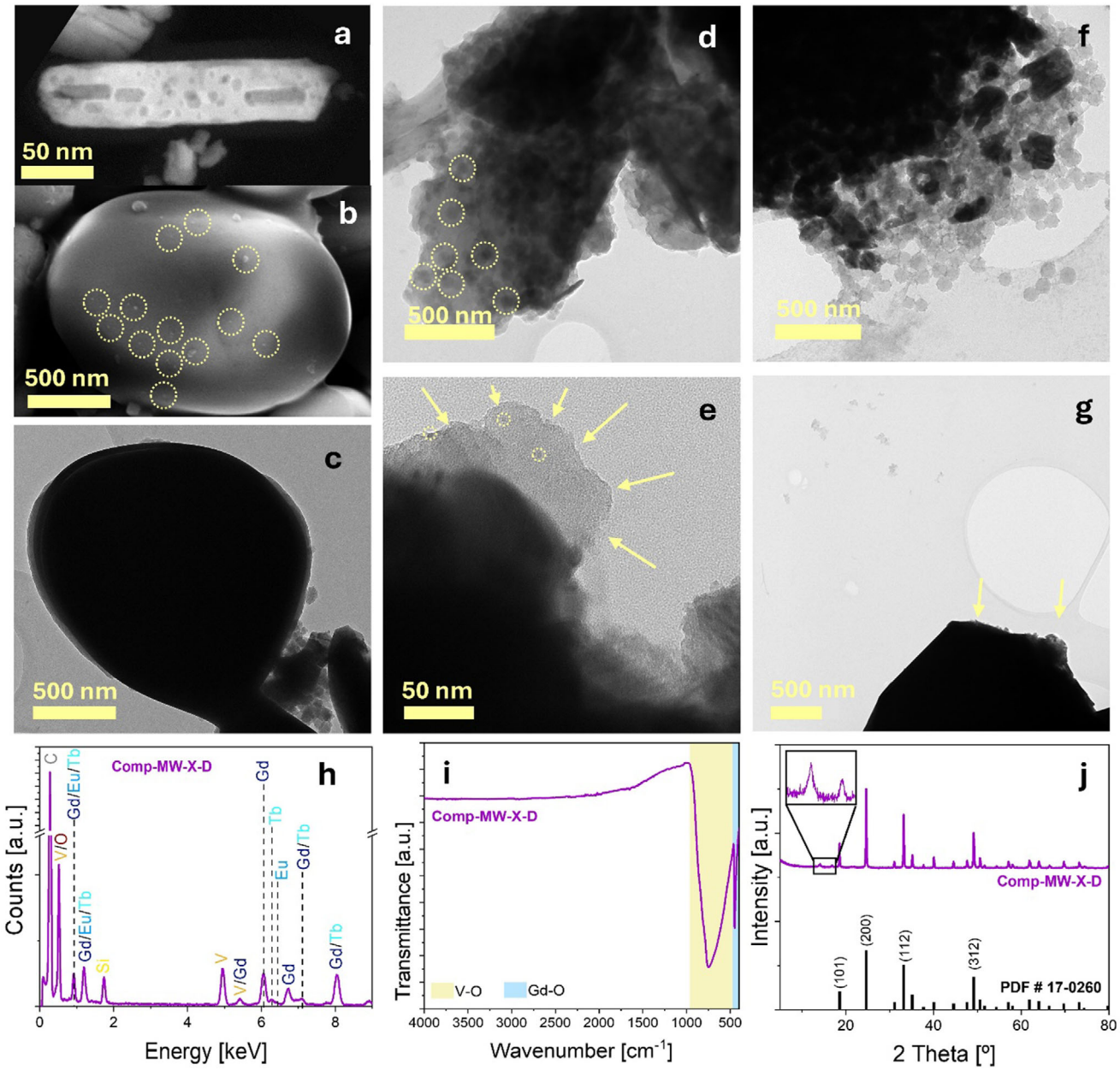

Figure 3. Morphological, structural and compositional characterization of composites. Morphological analysis of composites synthesized via different methods. a) TEM image and b) FESEM image of Comp-MW-X-D. TEM images of c) Comp-MW-H-D, d) Comp-MW-X-M, e) Comp-MW-H-M, f) Comp-HTC-X-M, and g) Comp-HTC-H-M. Dashed circles indicate the presence of CDs and the arrows highlight an organic matrix surrounding the Ln-NPs. Compositional characterization of Comp-MW-X-D: h) EDX spectrum confirming the elemental composition. i) FTIR spectra, where shaded yellow and blue regions indicate ν_s(V—O) and ν_s(Gd/Ln—O), respectively. j) XRD patterns, including the reference of PDF for tetragonal $GdVO_4$ (black).

Regarding CDs (Figure 4b), all samples displayed broad absorbance peaks at ≈260 nm, which might be attributed to $\pi \rightarrow \pi^*$ electronic transitions of C=C bonds in aromatic rings. Notably, CD-MW-X, exhibited a small shoulder at ≈350 nm which is likely associated to $\pi \rightarrow \pi^*$ transitions of C=O bonds.[39] Excitation spectra, however, were slightly red-shifted with respect to absorbance peaks. This discrepancy may be attributed to the surface states generated by oxygenated functional groups surrounding the CDs core[47] further supporting the amorphous polymeric nature of CDs (comprising sp^2 carbon domains and oxygen moieties) as previously determined by TEM.

Ln-NPs (Figure 4d), on the other hand, exhibited a single and narrow absorption peak in the UV region, which blue-shifted with increasing the Eu^{3+} doping concentration from 275 nm at 2% Eu to 248 nm at 5% Eu. This trend is consistent with literature reports attributing this band to $O^{2-} - Eu^{3+}$ charge transfer (CT).[48,49] Moreover, when monitoring excitation spectra at the emission of 618 nm, a broad band centered at 318 nm was

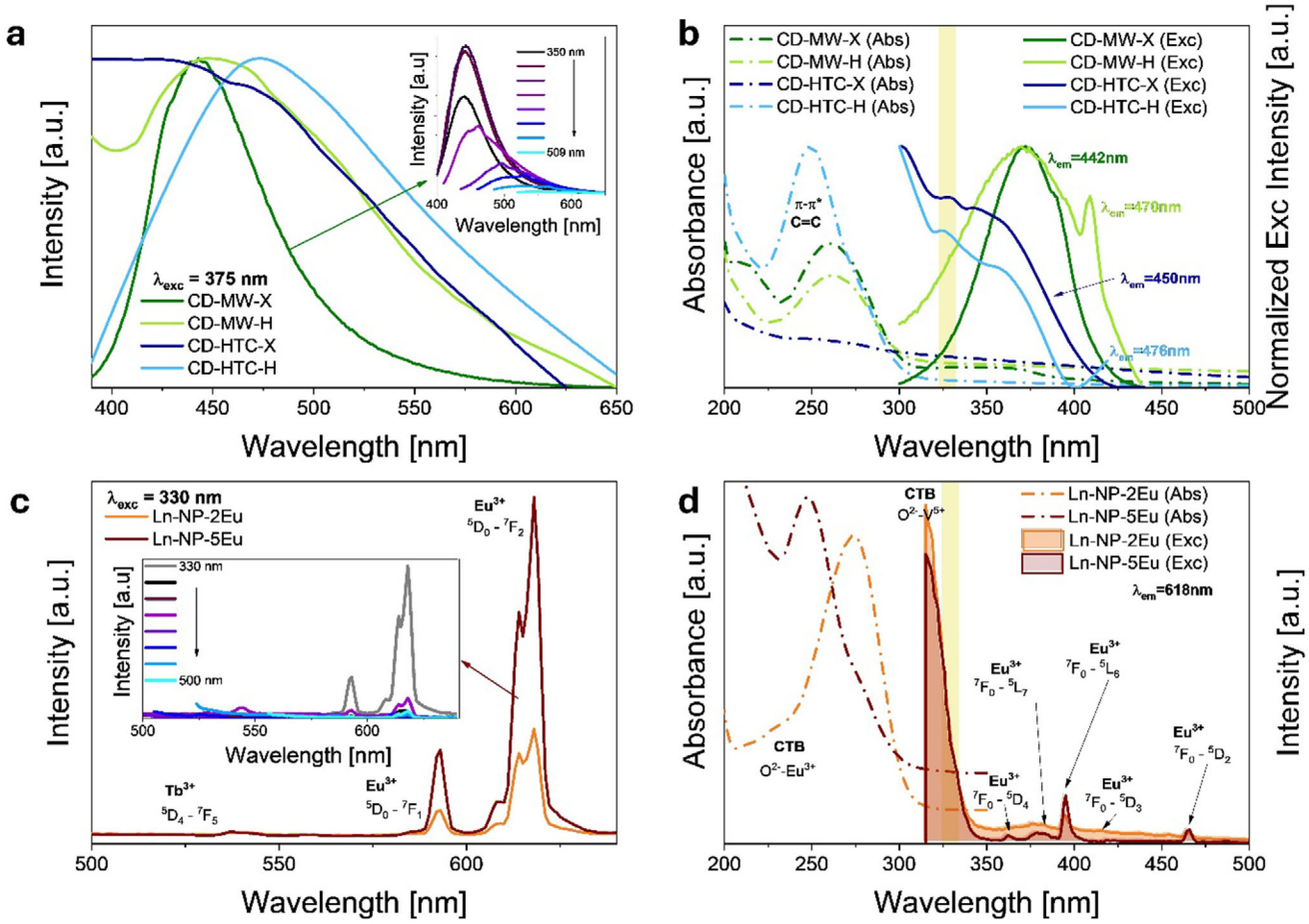

Figure 4. Optical properties of individual components. a) Normalized CDs emission spectra, with the inset showing the excitation-dependent emission of CD-MW-X. b) CDs absorbance (dashed-dotted lines) and excitation spectra (solid lines), with the yellow shading indicating the 330 nm wavelength. c) Emission spectra of Ln-NP-2Eu and Ln-NP-5Eu, with the inset displaying the emission of Ln-NP-5Eu at different excitation wavelengths. d) Ln-NPs absorbance (dashed-dotted lines) and excitation spectra (solid lines), with the yellow shading marking the 330 nm wavelength. Color legends specified into the graphs.

observed. As extensively reported, this feature corresponds to a CT transition from the *2p* orbital of O^2 to the *d* orbital of V^{5+}. Based on molecular orbital theory, this transition can be assigned to the $^1A_2(^1T_1)$ ground state to the $^1A_1(^1E)$ and $^1E(^1T_2)$ excited states of VO_4^{3-}.[50] Additionally, narrow peaks resulting from f-f transitions within the $4f^6$ configuration of the Eu^{3+} ions from the $^7F_0$ ground state to the $^5D_4$ (363 nm), $^5G_3$ (382 nm), $^5L_6$ (395 nm), $^5D_2$ (465 nm) were demonstrated to also contribute to the 618 nm red emission,[50,51] the most intense being the last two, which agrees with the emission profile in Figure 4c inset. Notably, the ratio between the intensities of the $O^{2-} - V^{5+}$ charge transfer band (CTB) and the f-f transitions is higher for Ln-NP-2Eu than for Ln-NP-5Eu (Table S2, Supporting Information). This suggests that at lower Eu^{3+} concentrations, the contribution of the CTB to the red emission is more important, whereas at higher Eu^{3+} concentrations, intrinsic Eu^{3+} transitions start playing a greater role. These findings align with the trends observed in absorption spectroscopy. Additionally, the weak or absent Tb^{3+} signal can be attributed to cross-relaxation energy transfer (CRET) processes, which become prominent at high Tb^{3+} concentrations. These non-radiative energy transfer mechanisms facilitate energy migration between neighboring Tb^{3+} ions, leading to concentration quenching effects that diminish observable Tb^{3+} emission.[52] Furthermore, Tb^{3+} acts as an intermediate in the energy transfer cascade, channeling excitation energy toward Eu^{3+} by repopulating its ^5D_J levels, thereby further reducing its own radiative emission.[53]

Since the excitation spectra of the individual components overlapped at 330 nm, this wavelength was selected to excite the composites and measure their PL emission spectra (**Figure 5**). Three main bands were identified: (i) a broad signal ranging from the UV to the green region, corresponding to the CDs emission, and (ii) two narrow peaks associated with the $^5Do \rightarrow {}^7F_1$and $^5Do \rightarrow {}^7F_2 \cdot Eu^{3+}$ transitions. [13]

Interestingly, the composites presented distinct PL behavior depending on the synthesis method, as revealed by comparing their emission profiles with those of the individual components. When CDs were integrated via hydrothermal deposition, the PL spectrum showed a lower intensity of the Eu^{3+} emission bands when compared to the pristine Ln-NP whereas the CDs

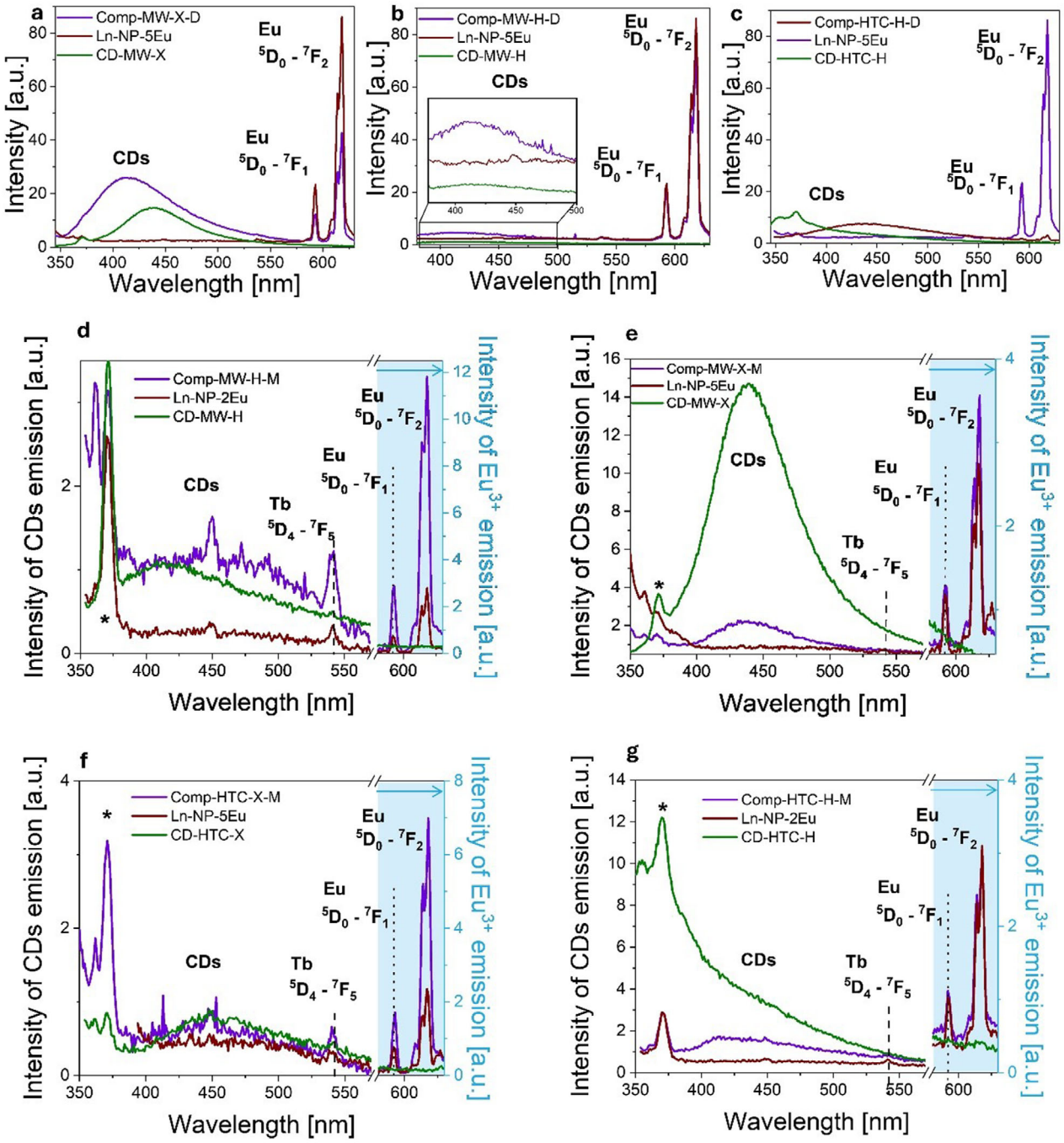

Figure 5. Photoluminescence (PL) emission spectra of composites and their individual components under 330 nm excitation. a) Comp-MW-X-D, b) Comp-MW-H-D, and c) Comp-HTC-H-D. d) Comp-MW-X-M, e) Comp-MW-H-M, f) Comp-HTC-X-M, and g) Comp-HTC-H-M. The X-axis in panels (d–g) is split to accommodate two Y-axes, allowing separate scaling for the CD emission (left axis) and Eu^{3+} emission (right axis), which differ markedly in intensity. Asterisks (*) denote the Raman peak of water.

emission intensified and slightly shifted (Figure 5a–c). In contrast, composites prepared by physical mixing either retained (Comp-MW-X-M and Comp-HTC-H-M) or enhanced (twofold in the case of Comp-HTC-X-M and fourfold for Comp-MW-H-M) the intensity of the ^{5}Do → $^7F_2$ · Eu^{3+} transitions, while the CDs emission significantly diminished (Figure 5d–g). While these variations might initially be attributed to differences in Ln-NP concentration and Eu^{3+} doping levels rather than the synthesis method, additional experiments provided further insights. Microwave-assisted hydrothermally deposited xylose-derived composites, prepared using varying concentrations of Ln-NP-2Eu and Ln-NP-5Eu (Figure S5, Supporting Information), exhibited emission trends consistent with those of other hydrothermally synthesized samples, characterized by a dominant CDs

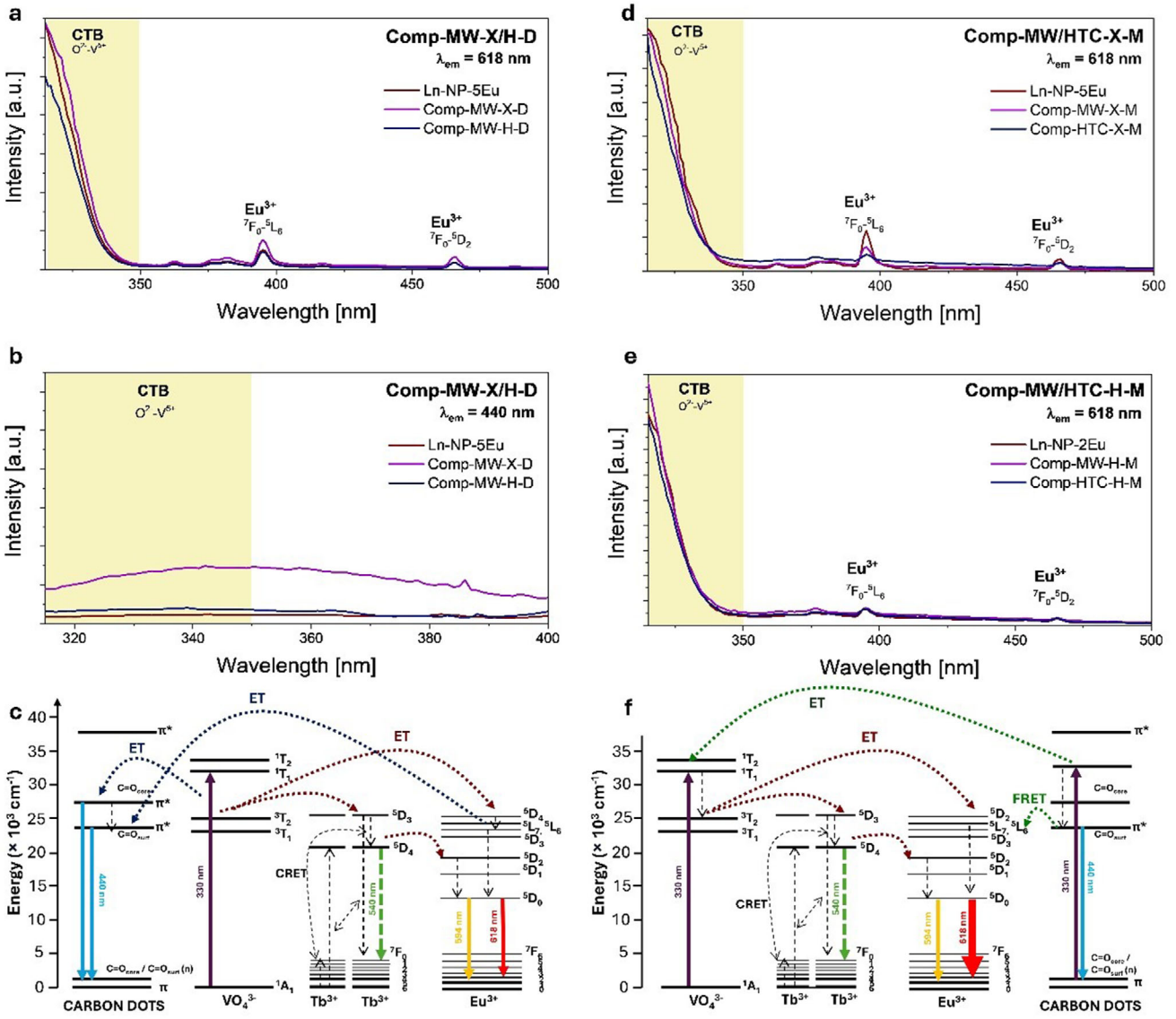

Figure 6. Elucidation of energy transfer mechanisms in the composites synthesized via a–e) hydrothermal deposition, and f–j) physical mixing. Excitation spectra of (a, b) Comp-MW-X-D, (c, d) Comp-MW-H-D, (f) Comp-MW-X-M, (g) Comp-MW-H-M, (h) Comp-HTC-X-M, and (i) Comp-HTC-H-M monitored at (a, c, f-i) 618 nm and (b, d) CDs emission (440 nm). Charge transfer bands (CTB) are highlighted with a yellow shadow and the f-f transitions of Eu^{3+} are labeled. Insets in (a, c, f–i) provide the ratio of integrated areas of CTB to $^7F_n \rightarrow {}^5L_6$ (C/L) and to $^7F_n \rightarrow {}^5D_2$ (C/D) as well as $^7F_n \rightarrow {}^5L_6$ to $^7F_n \rightarrow {}^5D_2$ (L/D) of both pristine Ln-NPs (red text) and composites (violet text). (e, j) Energy level diagrams illustrating the energy transfer (ET) pathways in the composites, including charge transfer, cross-relaxation (CRET), and Förster resonance energy transfer (FRET), emphasizing the role of CDs, VO_4^{3-}, Tb^{3+}, and Eu^{3+} in the luminescence process.

emission peak and a reduced lanthanide red emission. This suggests that the incorporation of Ln-NPs into the CDs precursor mixture leads to altered Ln-NP–CD interactions, ultimately influencing the PL properties as already speculated by Z. Shu et al.[44]

3.2.2. Energy Transfer Mechanism

These PL variations indicate the presence of two distinct energy transfer (ET) mechanisms governing the emission behavior of the composites. A comparative analysis of the excitation spectra of composites, pristine Ln-NPs and CDs is essential to elucidate these mechanisms (**Figure 6**). Also, **Table 2**, lists the ratio of the integrated areas for the different materials investigated in this paper.

Focusing first on the samples synthesized via hydrothermal deposition (Figures 6a–c;S6, Supporting Information), notable alterations in the excitation spectra relative to pristine Ln-NPs are observed. When monitoring the emission at 618 nm, the integrated intensity ratio of the VO_4^{3-}(CTB) to the f-f Eu^{3+}transitions (^7F_n→#x02075;$D_2$and $^7F_n \rightarrow {}^5L_6$) decreases upon the incorporation of CDs (values depicted as inset tables in Figure 6a–c). This indicates that intrinsic Eu^{3+}transitions contribute more significantly to the 618 nm emission in the composite, while the

Table 2. Ratio of integrated areas of CTB to $^7F_n \rightarrow {}^5L_6$, CTB to $^7F_n \rightarrow {}^5D_2$, and $^7F_n \rightarrow {}^5L_6$ to $^7F_n \rightarrow {}^5D_2$ of both pristine Ln-NPs and composites.

Sample	CTB / $^7F_0$is$^5L_6$	CTB / $^7F_0$–$^5D_2$	$^7F_0$–$^5L_6$ / $^7F_0$–$^5D_2$
Ln-NP-5Eu-2.5 mg mL^{-1}	34.2	116.9	3.4
Comp-MW-X-D	26.6	76.0	2.9
Comp-MW-H-D	31.8	98.7	3.1
Ln-NP-5Eu-0.25 mg mL^{-1}	20.7	71.2	3.4
Comp-MW-X-M	27.7	93.9	3.3
Comp-HTC-X-M	35.6	104.1	2.9
Ln-NP-2Eu-0.25 mg mL^{-1}	35.1	127.5	3.6
Comp-MW-H-M	35.0	120.4	3.4
Comp-HTC-H-M	31.1	108.3	3.5

CTB-mediated energy transfer becomes less dominant. Furthermore, the excitation spectrum monitored at the typical CDs emission (440 nm) exhibits an increase of the intensity of the band in the CTB region, suggesting that, after composite formation, CTB energy transfer is distributed between Ln ions and CDs (Figure 6e). This confirms that both emissive species compete for CTB-mediated energy transfer. Additionally, the decrease in the integrated intensity ratio value of the $^7F_n \rightarrow {}^5L_6$ to $^7F_n \rightarrow {}^5D_2$ (Insets of Figure 6a and c) transitions suggests that the $^7F_n \rightarrow {}^5L_6$ emission becomes less dominant in the composites. This is presumably due to a non-radiative energy transfer to CDs, facilitated by the close match between the energy of this level (25 316 cm^{-1}) and the CDs' expected energy gap (26 666 cm^{-1}) (Figure 6e). This interaction may also account for the enhanced and shifted CD emission observed after incorporation into the composites, (Figure 5a–c).

Similarly, composites produced via physical mixing also exhibit a decrease in the integrated intensity ratio of the $^7F_n \rightarrow {}^5L_6$ to $^7F_n \rightarrow {}^5D_2$ emissions compared to pristine Ln-NPs (Figure 6f–i), indicating interactions between CDs and Ln-NPs that confirm the successful formation of the composites. However, in this case, the energy transfer pathway appears to be reversed. Based on spectroscopic measurements—particularly the emission spectra of isolated CDs under 330 nm excitation (Figure S7, Supporting Information) and the excitation spectra of Ln-NPs and composites monitored at 618 nm (Figure 6f–i)—we infer that CDs act as sensitizers for the Eu^{3+} emissions in this case. They absorb energy in the UV–vis range and transfer it to the Ln-NP system via Förster Resonance Energy Transfer (FRET), facilitated by the spectral overlap, as previously reported.[13,21] This energy transfer, combined with that mediated by the vanadate group, ultimately enhances the intensity of the 618 nm emission (Figure 5d–g).

Notably, when evaluating the integrated intensity area ratio of CTB to lanthanide configurational transitions, composites derived from Ln-NP-5Eu exhibit an increase of the CTB/$^7F_n \rightarrow {}^5L_6$ ratio, whereas those synthesized from Ln-NP-2Eu show a decrease of this parameter. This suggests that in the former, CDs are attached to the Ln-NP surface in a way that optimally absorbs and transfers energy in the UV region, facilitating excitation of both the vanadate CTB and intrinsic Eu^{3+} transitions. In contrast, in the latter case, excitation in the visible range becomes more significant, broadening the absorption cross-section and promoting energy transfer from CDs to Eu^{3+} levels while reducing the contribution of CTB-mediated transfer (Figure S8, Supporting Information). This behavior can also be linked to the components' concentration, influencing the balance between energy transfer mechanisms.

Regardless of the Eu^{3+} doping content, composites synthesized via HTC exhibit more pronounced changes in excitation energy distribution when compared to pristine Ln-NPs than those obtained through MW-assisted methods. This would suggest a more effective integration of CDs in HTC-derived samples or that the concentration of the components favor the described phenomenon.

Since the ultimate goal is to use these composites as luminescent thermometric ratiometric sensors under 330 nm excitation—specifically by exciting the CTB and enabling the simultaneous detection of emissions from both Ln-NPs and CDs—their spectroscopic properties were evaluated under these conditions. The results indicate that Comp-HTC-X-M and Comp-MW-H-M exhibit a higher intensity for the 618 nm emission band (Figure 5e and f) correlated with a higher CTB/$^7F_n \rightarrow {}^5L_6$ intensity ratio values (inserted as a table in Figure 6g and h). This supports the proposed energy transfer mechanism, in which CDs and the vanadate group collectively absorb excitation energy. The subsequent energy transfer to Eu^{3+} levels via both conventional cascade processes and FRET increases the number of electrons transitioning from $^5D_n \rightarrow {}^7F_2$, ultimately leading to an intensified red emission (Figure 6j).

In both energy transfer mechanisms, Tb^{3+} plays a similar role, acting as a bridge to repopulate the ^5D_J levels of Eu^{3+}. Moreover, as previously discussed in Section 3.2.1, the high concentration of Tb^{3+} promotes CRET, ultimately leading to self-quenching. These two factors are responsible for the low emission intensity of Tb^{3+} at 536 nm.

3.2.3. CIE Chromaticity

After elucidating the energy transfer mechanisms, the chromaticity of each component was analyzed using the CIE (Commission Internationale de l'Éclairage 1971) coordinates (**Figure 7**). The results indicate that CDs exhibit blue emission, with those derived from hemicellulose positioned closer to the white reference point (0.33, 0.33). In contrast, Ln-NPs primarily emit in the red region, shifting towards the white reference as the Eu^{3+} doping concentration decreases. Composites, however, display intermediate chromaticity properties between their individual components, emitting in the violet-magenta region.

This dual-emission behavior, reflected in the CIE coordinates of the composites, highlights their potential use for applications requiring precise color tuning. In particular, their emission spanning from blue to red can be leveraged for the fabrication of advanced light-emitting devices, such as UV-excited white-light LEDs, where balanced broad- and narrow-band emissions are essential.[54,55] Moreover, the distinctive chromaticity of the composites under UV irradiation, combined with their solution-processability, makes them promising candidates for the development of anticounterfeiting inks and security labels.[20,44] The ability to modulate their emission profile through synthetic control offers additional opportunities for designing

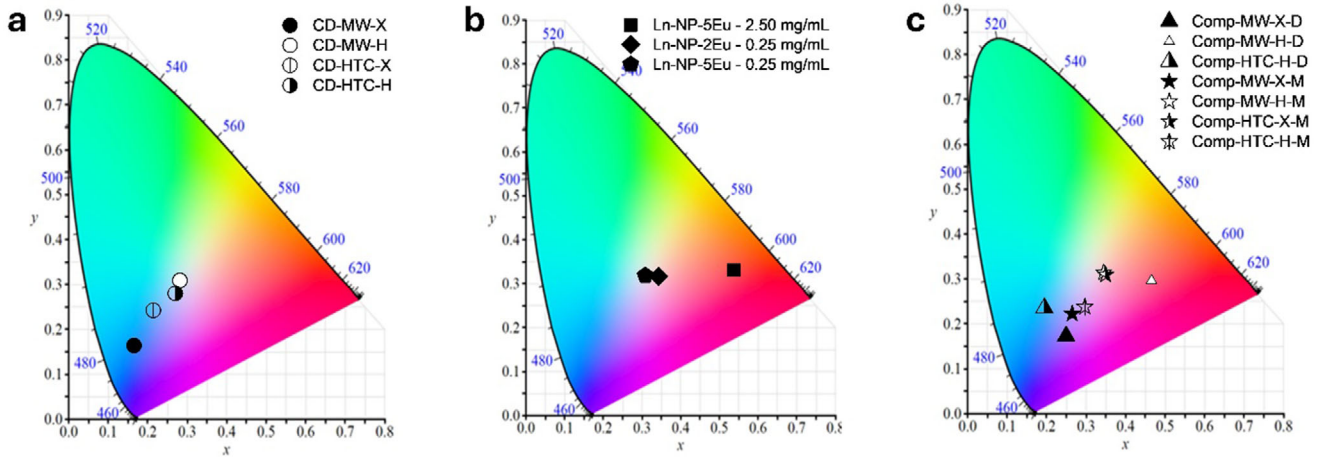

Figure 7. CIE coordinates of a) CDs, b) Ln-NP, and c) composites.

optical markers[56] and dynamic luminescent systems responsive to external stimuli.[57]

4. Application as Luminescent Thermometric Sensors

The temperature dependance of the PL emissions (in terms of integrated areas) of all the prepared materials was studied in the 298–358 K range under 330 nm excitation to assess their potential as luminescent thermometers.

4.1. Single-Band (SB) Luminescent Thermometric Sensors

As previously mentioned, CDs exhibit single broad band emissions between 350 and 650 nm under UV excitation, with intensity maxima at 420 and 470 nm, depending on the synthesis method. Upon increasing temperature, a decrease of the PL intensity is typically observed[14,58] due to the thermal activation of nonradiative decay processes[59,60] (Figures 8; S9, Supporting Information). The thermometric performance of CDs is evaluated through relative thermal sensitivity (S_R) and temperature resolution (δT).

S_R, described as the intensity variation rate of the designed probe at small changes in temperature, quantifies the rate of intensity variation with small temperature changes. δT is defined as the minimum resolvable temperature interval. These two parameters are given by Equations (1) and (2), respectively:[25]

$$S_R = \frac{1}{\Delta} \cdot \frac{\partial \Delta}{\partial T} \cdot 100 \quad (1)$$

$$\delta T = \frac{1}{S_R} \cdot \frac{\delta \Delta}{\Delta} \quad (2)$$

where Δ is the thermometric parameter (PL intensity or intensity ratio in this study), $\frac{\partial \Delta}{\partial T}$ is the derivative of Δ with respect to temperature, and $\frac{\delta \Delta}{\Delta}$ is the uncertainty of Δ determination.

This uncertainty arises from factors such as the experimental setup, the detector characteristics, and the integration time employed during the spectral acquisition. In all calculations, $\delta\Delta/\Delta$ was set to 0.5%, a value commonly adopted in the literature as a compromise reflecting typical experimental conditions.[25]

As shown in **Figure 8**, the PL intensity decrease of CD-MW-X and CD-HTC-H follows a linear trend as the temperature increases in the range of 308–358 K and delivers maximum S_R values of 1.49% K^{-1} and 0.82% K^{-1} at 358 K, respectively. These values are similar to some reported in the literature[61–63] but still below those of state-of-the-art luminescent thermometers[10,60] (see Table S3, Supporting Information). Conversely, CD-MW-H and CD-HTC-X (Figure S9, Supporting Information) exhibited poorer correlations along the evaluated temperature range, limiting their thermometric performance (Figure 8e).

For Ln-NP-5Eu, the emission intensity integrated area variations corresponding to the Tb^{3+} $^5D_4 \rightarrow {}^7F_5$ (536 nm), Eu^{3+} $^5D_0 \rightarrow {}^7F_1$ (593 nm) and Eu^{3+} $^5D_0 \rightarrow {}^7F_2$ (618 nm) transitions were also analyzed under the same conditions (**Figure 9**). A decrease in intensity when the temperature increased was clearly observed for both Eu^{3+}- related transitions (Figure 9a). When normalized to the maximum of intensity, they followed a similar linear trend (Figure 9b), yielding a maximum S_R of 1.87% K^{-1} at 358 K (Figure 9c), a value comparable to that of other similar single-band luminescent thermometers reported in the literature (Table S4, Supporting Information).[64] However, in the case of Tb^{3+}, the integrated emission area fluctuated by less than 20% across the entire temperature range and did not fit any simple mathematical function (Figure 9b), rendering it unsuitable for use as a SB luminescent thermometer.

4.2. Ratiometric (R) Luminescent Thermometric Sensors

Because of their simplicity, SB approaches present certain limitations, as their accuracy is often affected by external factors such as environmental interferences (e.g., changes in surrounding medium), power fluctuation or illumination oscillations of the excitation source, the signal-to-noise ratio and instabilities in the detection set-up system, the absorption and scatter cross-sections of the emitters, the variation of the concentration of emitters in the sample where the temperature is going to be

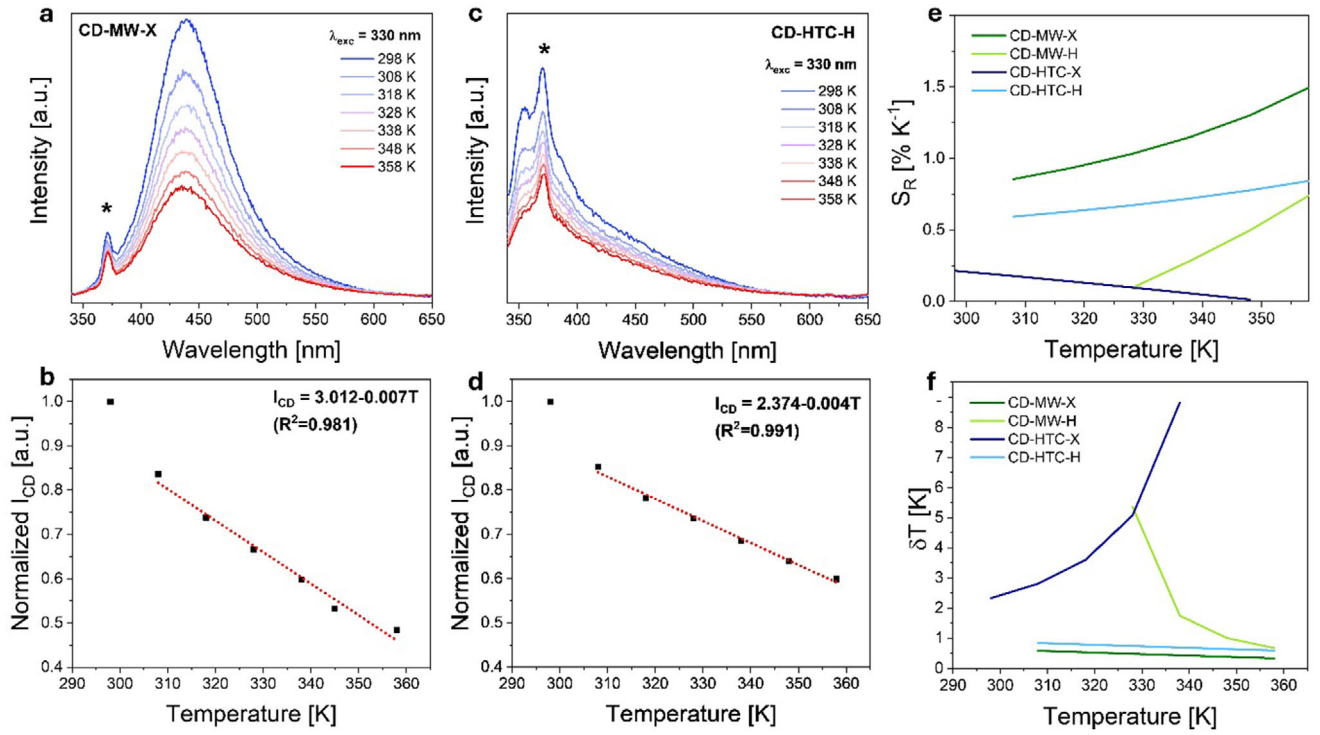

Figure 8. Luminescent nanothermometric performance of synthesized CDs. PL spectra recorded at 330 nm for temperatures from 298 K to 358 K for a) CD-MW-X and c) CD-HTC. Temperature-dependent fitting of normalized emission intensities for b) CD-MW-X and d) CD-HTC, e) relative thermal sensitivities ($\mathbf{S}_R$), and f) temperature resolutions (δT) of CDs tested as single-band (SB) luminescent thermometers. The (*) in (a) and (c) labels the Raman peak of water.

measured, or the inhomogeneity on the distribution of the emitters in the luminescent thermal probes.[25] To mitigate these shortcomings, ratiometric (R) thermometry offers a more robust alternative. This method relies on the intensity ratio of two emission bands, thereby introducing an internal reference that enhances measurement reliability and minimizes matrix dependency.

To explore this approach, the luminescent thermometric performance of pristine Ln-NP-5Eu was first evaluated using the intensity ratio of the emissions corresponding to the Eu^{3+} ($^5D_n \rightarrow {}^7F_2$)/($^5D_n \rightarrow {}^7F_1$) and Eu^{3+} ($^5D_n \rightarrow {}^7F_2$)/$Tb^{3+}$ ($^5D_4 \rightarrow {}^7F_5$) transitions. As depicted in Figure 9d the Eu^{3+} ($^5D_n \rightarrow {}^7F_2$)/($^5D_n \rightarrow {}^7F_1$) calibration exhibited a poor correlation, and the calculated thermometric parameters were suboptimal, indicating that this system is not well-suited for ratiometric sensing (Figure 9e). By contrast, the Eu^{3+} ($^5D_n \rightarrow {}^7F_2$)/$Tb^{3+}$ ($^5D_4 \rightarrow {}^7F_5$) intensity ratio demonstrated significantly better performance, showing excellent agreement with an exponential fit (R^2 = 0.999, Figure 9d) and yielding a maximum S_R of 2.39% K^{-1} at 298 K (Figure 9e), a value comparable to those reported in the literature (Table S4, Supporting Information), with the added advantage of being achieved at relatively low temperature.[53,64,65]

The integration of CDs onto Ln-NPs to form composite materials introduced an additional emissive center into the system. Given the nature of CDs, significant differences in thermometric behavior (such as distinct intensity decreasing rate) were anticipated compared to pristine Ln-NPs. To assess the ratiometric thermometric performance of the composites, the emission peak of CDs in the blue region of the visible spectrum and the 618 nm emission peak corresponding to the $^5D_0 \rightarrow {}^7F_2$ transition of Eu^{3+} were analyzed. Initially, the evolution of individual emissions with temperature was examined. In both cases, emission intensity decreased upon heating, but the signal decay rate and the two components' relative proportions varied among samples (**Figures 10** and 11). These differences, along with the deviations from the behavior of individual isolated components (Figure S10, Supporting Information), suggest an interaction between CDs and Ln-NPs that alters the energy transfer mechanisms within the composites when compared to those observed in pristine Ln-NPs. This observation aligns with the spectroscopic data presented in previous sections and further supports the successful formation of the composites.

Interestingly, for the composites prepared by physical mixing (Figure 10) – except for Comp-HTC-H-M – the 618 nm emission intensity remained largely stable, with variations below 10% between the highest and lowest values. Considering that pristine Ln-NPs exhibit an intensity reduction to 50% of their original emission when heated from 298 K to 358 K, this suggests that the incorporation of CDs enhances the thermal stability of the $^5D_0 \rightarrow {}^7F_2$ Eu^{3+} emission. In contrast, the composites obtained via hydrothermal deposition (Figure 11) exhibited a more pronounced decrease of the emission intensity of the band located at 618 nm (the most important decrease corresponding to Comp-MW-X-D, with a 75% diminishment of the original intensity), while the CD

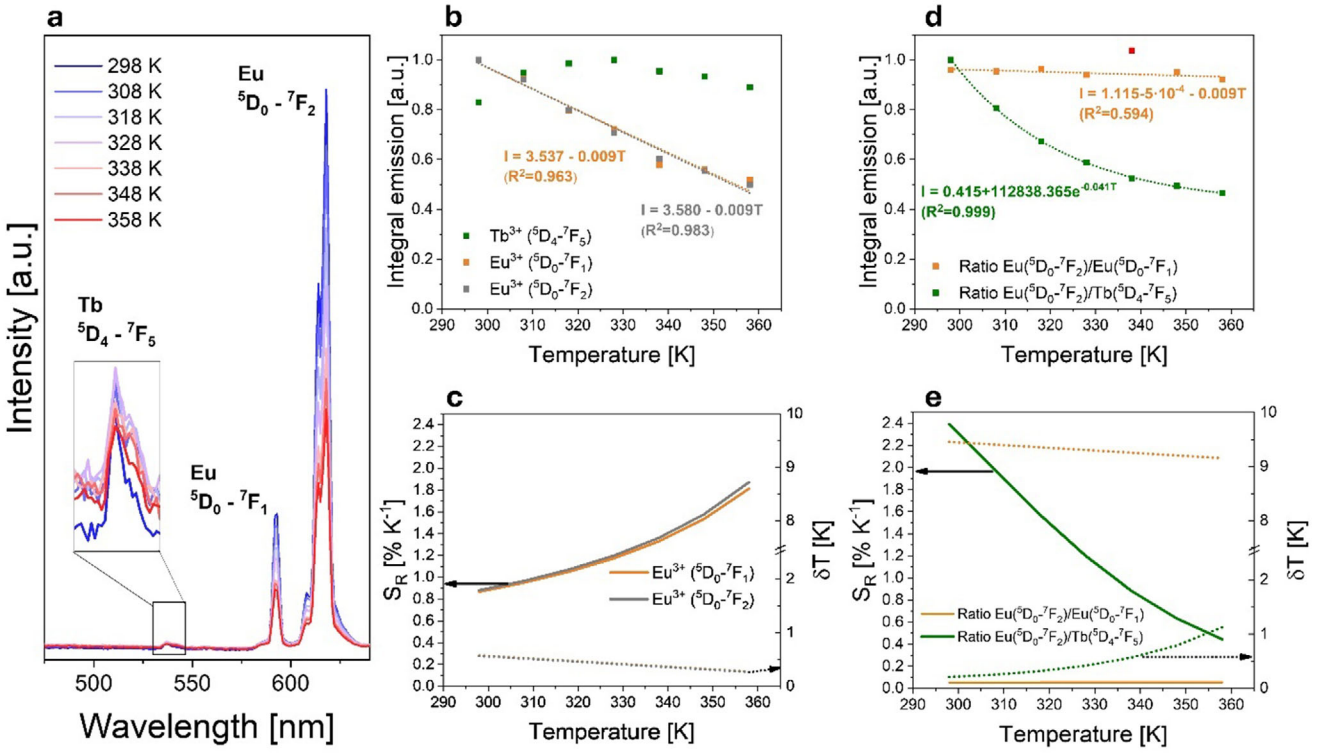

Figure 9. Luminescent thermometric performance of Ln-NP-5Eu. a) PL spectra recorded under 330 nm excitation at temperatures ranging from 298 K to 358 K. b, d) Temperature-dependent analysis of normalized integrated emission intensities for: (b) individual transitions—Tb^{3+}: $^5D_4 \rightarrow {}^7F_5$ (536 nm), Eu^{3+}: $^5D_n \rightarrow {}^7F_1$ (593 nm), and Eu^{3+}: $^5D_n \rightarrow {}^7F_2$ (618 nm); and (d) intensity ratios—Eu^{3+} ($^5D_n \rightarrow {}^7F_2$)/($^5D_n \rightarrow {}^7F_1$) and Eu^{3+} ($^5D_n \rightarrow {}^7F_2$)/$Tb^{3+}$ ($^5D_4 \rightarrow {}^7F_5$). c, e) Calculated thermometric parameters: relative thermal sensitivity (S_R, solid lines) and temperature resolution (δT, dashed lines) for: (c) SB approach and (d) R strategy. Color coding is indicated within each graph.

emission showed relatively lower variability compared to that of the Ln-NPs.

Following this initial evaluation, the intensity ratio of the Eu^{3+} ($^5D_n \rightarrow {}^7F_2$)/($^5D_n \rightarrow {}^7F_1$) transitions was calculated and assessed as thermometric parameter for thermometric approach over the 298–358 K temperature range (Figures 10 and 11). Since this ratio is derived from a phenomenological expression, modeling the composite behavior is complex, and the operational temperature range must be carefully adjusted for reliable application.[66] In the regions where intensity correlates with temperature, exponential fittings are generally observed, which agrees with most of the published works.[13,16,17,66–68] An exception is Comp-HTC-D-H, which exhibits a second-degree polynomial fit.

The analysis of the ratiometric thermometric performance (**Figure 12**), revealed promising results across all composite materials, with maximum relative thermal sensitivities (S_R) exceeding 0.80% K^{-1}. In general, hydrothermally deposited composites outperformed physically mixed ones, demonstrating optimal performance at higher temperatures, whereas physically mixed samples exhibited better performance at lower temperatures. However, Comp-HTC-H-M emerged as the best-performing composite, with the broadest operational temperature range (298–358 K) and the highest S_R (5.62% K^{-1}). Comp-MW-X-D followed closely, achieving the same maximal S_R but within a narrower effective temperature range (318–348 K). These results surpass those of previously reported CD-containing luminescent thermometric composites (Table S5, Supporting Information).[13–17]

Furthermore, to assess the signal stability of one of the most promising materials (Comp-MW-X-D), which exhibited a relative thermal sensitivity of up to 5.6% K^{-1}, we monitored the evolution of the ratiometric intensity between the CD emission peak and the Eu^{3+} $^5D_n \rightarrow {}^7F_2$ transition. Measurements were performed under continuous 330 nm excitation while maintaining the sample at a constant temperature of 348 K over a 75-minute period. The ratiometric signal demonstrated good temporal stability, with a maximum fluctuation of approximately 15% between the highest and lowest recorded values, as can be seen in **Figure 13**.

5. Conclusion

In this study $GdVO_4$:Tb,Eu/CD composites were successfully prepared by two different synthetic procedures: hydrothermal deposition and physical mixing. The Ln-NPs counterparts were synthesized via a soft hydrothermal procedure from Ln-chlorides, while biomass-related reactants, including commercial xylose or almond-shell extracted hemicellulose, were employed as CDs precursors. The composite formation was initially inferred by morphological and compositional characterization and demonstrated by spectroscopic studies. The fabrication methodology, that at its time influences the concentration of CDs in the

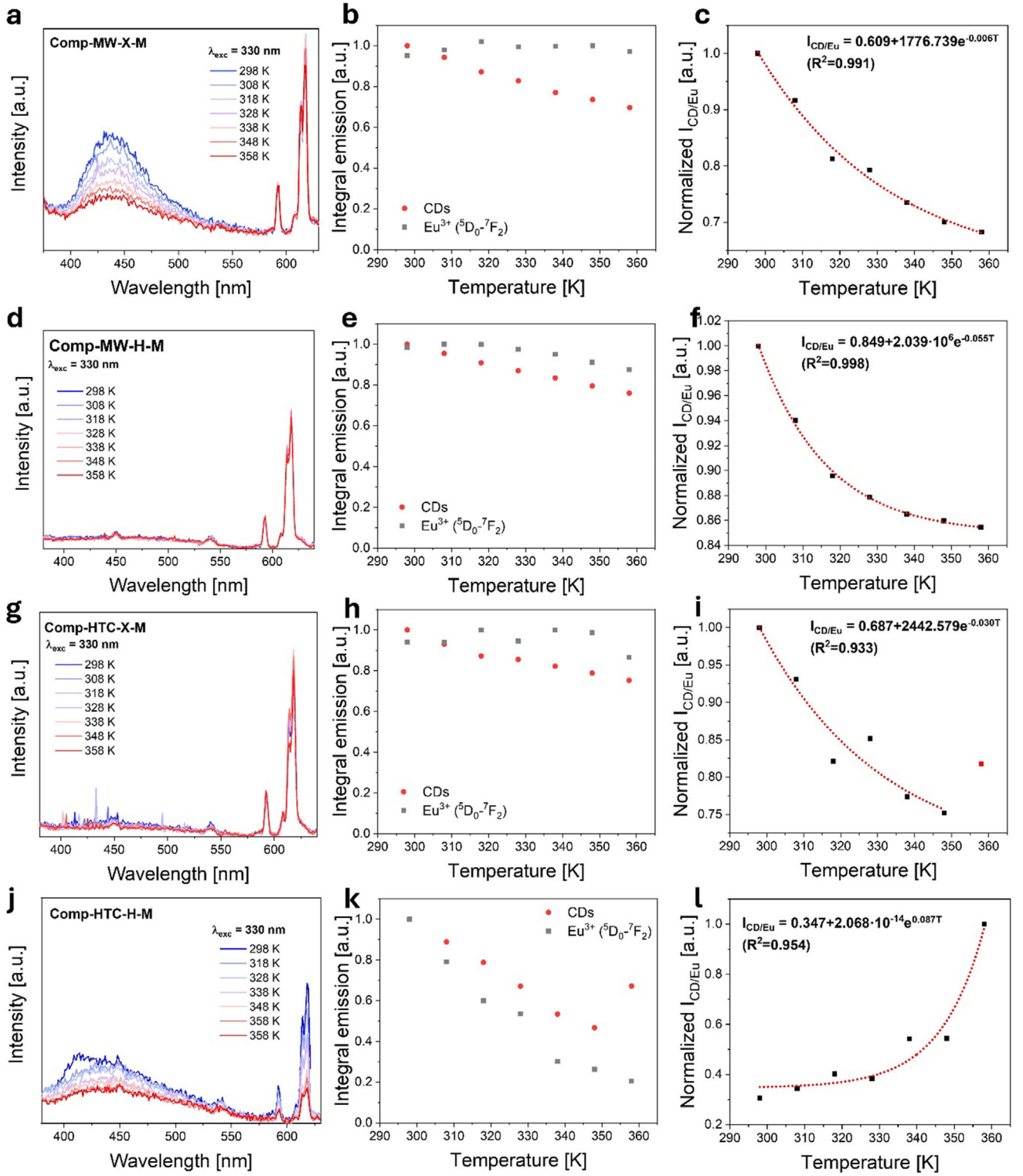

Figure 10. Temperature-dependent photoluminescence (PL) intensity variation of composites synthesized via physical mixing. a, d, g, j) PL spectra recorded by exciting at 330 nm for temperatures ranging from 298 K to 358 K, b, e, h, k) normalized emission intensities of CDs and Eu^{3+} ($^5D_n \rightarrow {}^7F_2$) as a function of temperature, and c, f, i, l) normalized intensity ratio (I_{CD}/I_{Eu}) versus temperature fittings for (a–c) Comp-MW-X-M, (d–f) Comp-MW-H-M, (g–i) Comp-HTC-X-M, and (j–l) Comp-HTC-H-M.

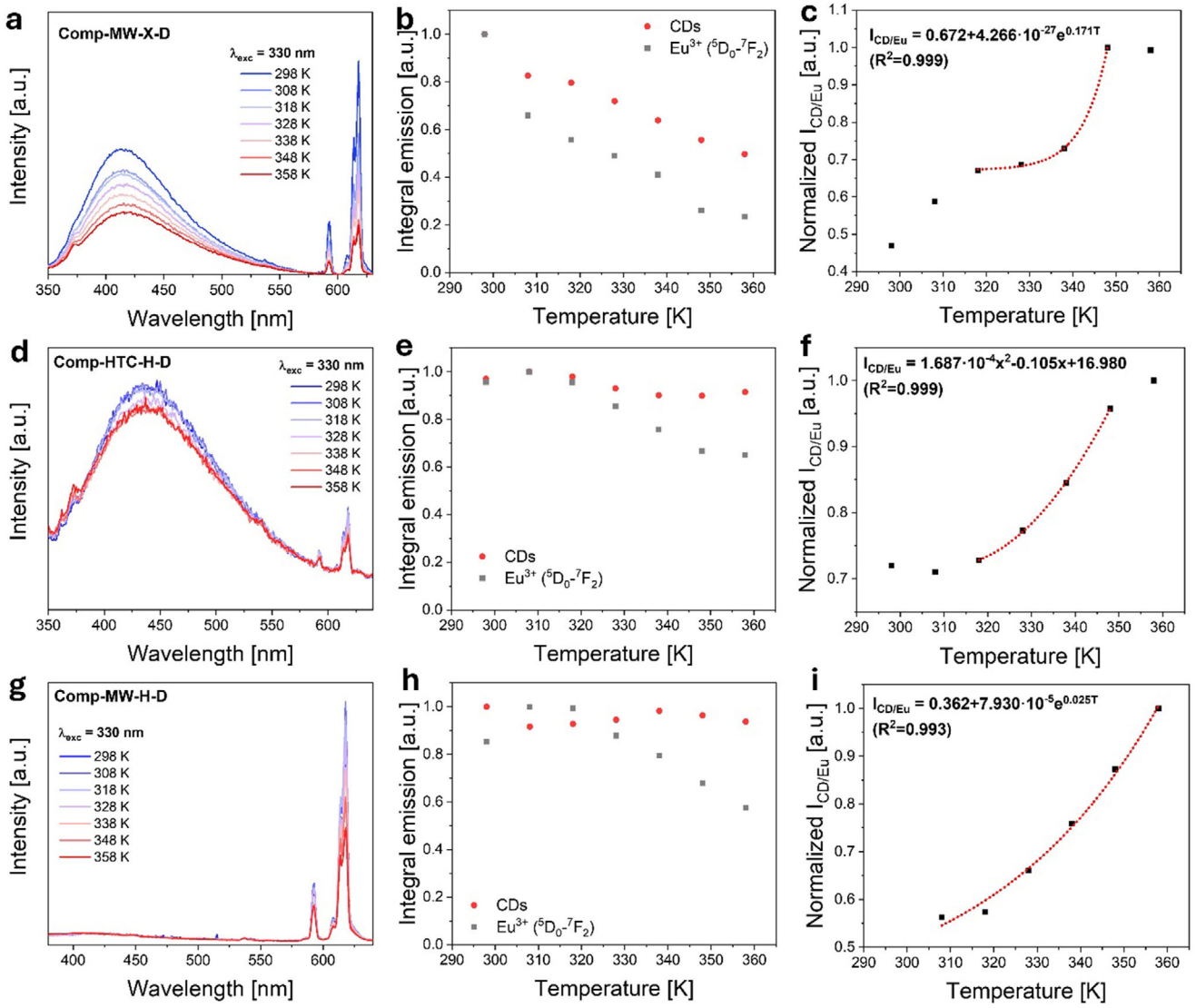

Figure 11. Temperature-dependent photoluminescence (PL) intensity variation of composites synthesized via hydrothermal deposition. a, d, g) PL spectra recorded after excitation at 330 nm for temperatures ranging from 298 K to 358 K, b, e, h) normalized emission intensities of CDs and Eu^{3+} ($^5D_n \rightarrow {}^7F_2$) as a function of temperature, and c, f, i) normalized intensity ratio (I_{CD}/I_{Eu}) versus temperature fittings for (a–c) Comp-MW-X-D, (d–f) Comp-MW-H-D, (g–i) Comp-HTC-H-D.

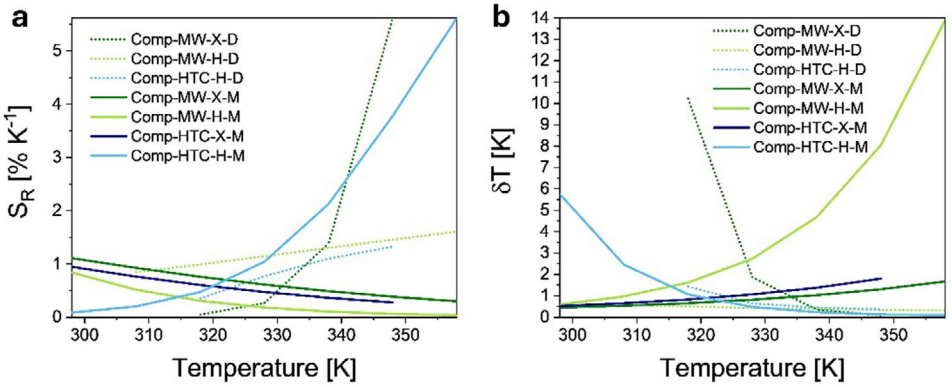

Figure 12. Performance of composites as ratiometric temperature sensors. a) Relative thermal sensitivities (S_R), and b) temperature resolutions (δT).

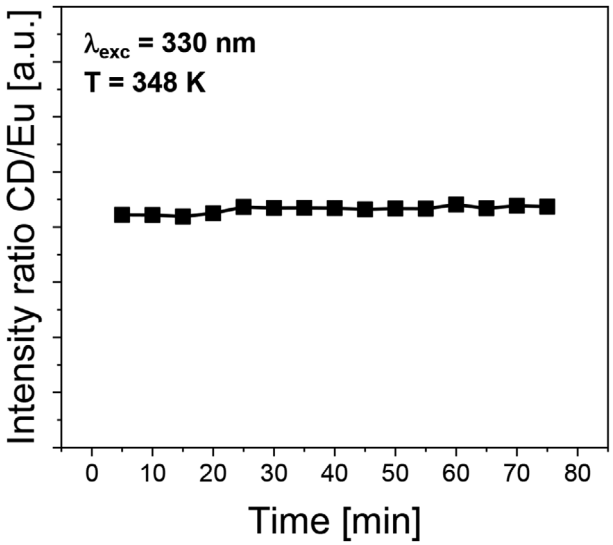

Figure 13. Temporal stability of the ratiometric intensity signal of Comp-MW-X-D over 75 minutes at 348 K.

final products, played a crucial role in defining the energy transfer mechanisms governing the photoluminescent properties of the materials. In hydrothermally deposited samples, competitive energy transfer between Eu^{3+} and CDs from VO_4^{3-} led to a decrease in the $^5D_n \rightarrow {}^7F_2$ Eu^{3+} emission intensity compared to pristine lanthanide-doped nanoparticles. Conversely, CDs acted as sensitizers in physically mixed composites, enhancing Eu^{3+} red emission through a cooperative energy transfer mechanism.

The dual-emissive nature of the composites results in violet-magenta chromaticity, intermediate between the blue CDs and red-emitting Ln-NPs, enabling their use in tunable optical applications.

The luminescent thermometric performance of all synthesized materials—including CDs, lanthanide-doped nanoparticles, and their composites—was systematically evaluated. Among them, the composites exhibited the best performance as luminescent thermometers under a ratiometric approach. Notably, the champion composite (Comp-HTC-H-M) demonstrated outstanding temperature sensing capabilities over the 298–358 K range, achieving a maximum relative thermal sensitivity of 5.6% K^{-1} at 358 K. These results underscore the strong potential of CD-based lanthanide composites for advanced luminescent thermometry applications in areas such as optoelectronics, microfluidics, and healthcare. Their operational temperature range, combined with excellent water dispersibility, makes them particularly well-suited for real-time temperature mapping in microfluidic channels. This could be useful for the alimentary industry or environmental protection, thanks to the possibility of photothermal detection of additives and contaminants such as azo-dye Amaranth.[69] Furthermore, embedding the composites in polymeric or hydrogel matrices—such as polyacrylamide or polyvinyl alcohol—opens the door to the development of smart, wearable sensors. When integrated with a compact UV excitation source and photoluminescence detector[70] or combined with flexible optical fibers,[71,72] these materials could enable continuous, non-invasive monitoring of body temperature, offering promising applications in personalized healthcare and biomedical diagnostics.

6. Experimental Section

Materials: D-(+)-Xylose (≥99%) was purchased from Sigma-Aldrich, and sulfuric acid (95–98%) was obtained from Scharlab. Hemicellulose was extracted from crushed almond shells (supplied by Unió Nuts) via microwave-assisted acidic hydrolysis. Gd_2O_3 (99.999%) was sourced from Thermo Fisher Scientific, NH_4OH (30%) and (HCl 37% QP) from Panreac, and Tb_4O_7 (99.9%), Eu_2O_3 (99.99%), and NH_4VO_3 (99%) from Strem Chemicals.

Ln-NP Synthesis: Crystalline nanoparticles of $GdVO_4$ doped with Tb^{3+} (15 at%) and Eu^{3+} (2, 5 at%) were prepared following a soft hydrothermal synthesis method. Ln-chlorides were first prepared by dissolving the required stoichiometric amounts of Ln-oxides (Gd_2O_3, Tb_4O_7, and Eu_2O_3) in a hydrochloric acid solution (distilled H_2O (15 mL):HCl 37% (5 mL)), and heating the solution until complete dryness. Then, these Ln-chlorides were dissolved in distilled H_2O (10 mL), and added to a solution of NH_4VO_3 (with a 3% excess over the stoichiometric required amount) in distilled (DI) water (20 mL), with the pH adjusted to 9 by addition of diluted NH_4OH (30%), under magnetic stirring for 1 h. In each case, the light yellow dispersion formed was heated in a Teflon-lined autoclave at 463 K for 24 h. The resulting product was collected by centrifugation, washed with DI water several times, and dried overnight at 393 K. Finally, the samples were annealed at 1173 K for 24 h to remove surface defects formed during the low-temperature synthesis process and to promote a higher degree of crystallization.

CD-MW Synthesis: CD-MW were synthesized via a microwave-assisted hydrothermal method. Briefly, precursor (0.5000 g) – either commercially available xylose (CD-MW-X) or almond-shell-extracted hemicellulose (CD-MW-H) – was dissolved in 20 mL of DI water. The solution was then transferred to a 100 mL reactor and heated to 160 °C for 20 minutes using a flexiWAVE microwave system. After the reaction, the mixture was allowed to cool naturally through the equipment's ventilation system. The product was purified by mechanical filtration using a polytetrafluoroethylene (PTFE) syringe filter (0.22 µm), followed by dialysis against DI water (1 L) for 48 hours using a regenerated cellulose membrane (molecular weight cutoff (MWCO) 1 kDa), with the dialysate replaced every 24 hours.

CD-HTC Synthesis: CD-HTC were synthesized using a conventional hydrothermal method. In a typical procedure, precursor (0.5000 g) – either commercially available xylose (CD-HTC-X) or almond-shell-extracted hemicellulose (CD-HTC-H) – was dissolved in DI water (20 mL). The solution was then transferred to a 100 mL Teflon-lined autoclave reactor and heated at 180 °C for 12 hours in a conventional stove. After the reaction, the mixture was allowed to cool naturally. The resulting product was purified by mechanical filtration using a PTFE syringe filter (0.22 µm), followed by dialysis against DI water (1 L) for 48 hours using a regenerated cellulose membrane (molecular weight cutoff (MWCO) 1 kDa), with the dialysate replaced every 24 hours.

Comp-MW-X/H-D Synthesis: Comp-MW-X/H-D composites were synthesized via microwave-assisted hydrothermal deposition of CDs onto $GdVO_4$:15 at. % Tb:2–5 at. % Eu nanoparticles (Ln-NPs). Briefly, predetermined amounts of Ln-NPs were mixed with precursor (0.5000 g) – either commercial xylose (Comp-MW-X-D) or almond-shell-extracted hemicellulose (Comp-MW-H-D) – and DI water (20 mL) to prepare solutions with NP concentrations of 1%, 2.5%, 5%, and 10% in weight. Each solution was transferred to a 100 mL reactor and heated at 160 °C for 20 minutes using a flexiWAVE microwave system. Following natural cooling, the resulting mixtures were filtered through a PTFE filter (0.22 µm). The collected solids were subsequently dried, and redispersed in DI water.

Comp-HTC-X/H-D Synthesis: Comp-HTC-X/H-D composites were synthesized via hydrothermal treatment. In this process, $GdVO_4$:15at.% Tb:5at.% Eu NPs (0.0500 g) were mixed with 0.5000 g of precursor – commercial xylose (Comp-HTC-X-D) or almond-shell-extracted hemicellulose (Comp-HTC-H-D) and Milli-Q water (20 mL) to prepare a solution with a 10% Ln-NP concentration. The mixture was transferred to a 100 mL

Teflon-lined autoclave and heated at 180 °C for 12 hours. Following natural cooling, the resulting mixture was filtered through a PTFE filter (0.22 µm). The collected solids were dried, and redispersed in DI water. Due to the impossible separation of Comp-HTC-X-D and some byproducts that quenched the PL of the composite, the sample was discarded for this study.

Comp-MW/HTC-X/H-M synthesis: Comp-MW/HTC-X/H-M composites were prepared by physically mixing CD-MW or CD-HTC with $GdVO_4$:15at.% Tb:2-5at.% Eu NPs. Specifically, concentrations of 1% (relative to the initial precursor weight) were achieved by adding Ln-NPs (0.0050 g) to the CD solution, followed by continuous stirring for 4 hours at room temperature. Ln-NP-5Eu were used for Comp-MW/HTC-X-M while Ln-NP-2Eu were employed for Comp-MW/HTC-H-M. In the case of Comp-HTC-X-M a small variation of the procedure was applied: the CD-HTC-X solution was diluted 1:90 (v/v) in DI water prior to mixture with Ln-NPs to reduce absorbance and prevent the PL quenching by inner-field effect.

Characterization: The morphology and composition of the as-prepared samples were analyzed by a JEOL F200 transmission electron microscope operated under an accelerated voltage of 200 kV and equipped with a Centurio EDX detector. A FEI Scios 2 scanning electron microscope operating at 30 kV was used to evaluate surface texture of the samples. XRD patterns for structure elucidation were recorded with a Bruker-AXS D8-Advanced X-Ray Diffractometer using Cu Kα radiation ($\lambda = 0{,}154$ nm) and a 1D LYNXEYE-XE-T detector in the 0 to 80 ° range and interpreted with the DIFFRAC.EVA V5.2 X-Ray Diffraction software. A Jasco FT/IR-6700 Infrared Spectrometer equipped with a Diamond Attenuated Total Reflective (ATR) Crystal and measuring along the 4000–500 cm^{-1} energy range was employed to elucidate the functional groups present in the samples. Optical absorption spectra were obtained at 0.5 nm step, 10 s integration time, using a deuterium lamp in Cary Series 5000 UV-vis-NIR Spectrometer from Agilent Technologies. Fluorescence measurements were carried out on a Fluorolog Horiba Jobin Yvon Spectrofluorimeter equipped with a photomultiplier detector, double monochromator and a Xenon light source. The spectra were collected at 1.00 nm step, 0.10 s integration time and with the slits opened 3 nm (both for the emission and excitation monochromators). A Rapid Peltier-based temperature-controlled sample holder was used for temperature dependent PL measurements. The 298–358 K temperature range was evaluated in 10 K steps (2 minutes of stabilization between measurements). Agitation at 3500 rpm was set to prevent composites precipitation.

Supporting Information

Supporting Information is available from the Wiley Online Library or from the author.

Acknowledgements

This work was supported by MCIN/AEI/10.13039/501100011033 through Grant PID2021-128090OB-C21-C22, co-funded by ERDF ("A way of making Europe"), and TED2021-129487B-C31 funded by MICIU/AEI/10.13039/501100011033 and European Union NextGenerationEU/PRTR. RSM was supported, partially, by Diputació de Tarragona through project 2024DIPTA-URV-PIN01. LFR was supported by NextGenerationEU/Catalunya 2023 INV-2 00033-ID11.

Conflict of Interest

The authors declare no conflict of interest.

Data Availability Statement

The data that support the findings of this study are available from the corresponding author upon reasonable request.

Keywords

carbon dots, composites, europium, lanthanide-doped nanoparticles, luminescent thermometry

Received: May 8, 2025
Revised: July 25, 2025
Published online: September 12, 2025

[1] X. Xu, R. Ray, Y. Gu, H. J. Ploehn, L. Gearheart, K. Raker, W. A. Scrivens, *J. Am. Chem. Soc.* **2004**, *126*, 12736.
[2] L. Đorđević, F. Arcudi, M. Prato, *Nat. Protoc.* **2019**, *14*, 2931.
[3] X. Liao, C. Chen, R. Zhou, Q. Huang, Q. Liang, Z. Huang, Y. Zhang, H. Hu, Y. Liang, *Dyes Pigm.* **2020**, *183*, 108725.
[4] X. Wang, Q. Zhao, Q. Song, H.e Bu, J. Gao, L. Li, X. Yu, X. Yang, Z. Lu, X. Zhang, *Spectrochim. Acta, Part A* **2024**, *310*, 123952.
[5] X. Liu, J. Zheng, C. Wei, Z. Wang, Y. Yang, L. Yan, X. Liu, B. Xu, *Adv. Opt. Mater.* **2024**, *12*, 2400274.
[6] Y. K. Jung, E. Shin, B.-S. Kim, *Sci. Rep.* **2015**, *5*, 18807.
[7] Y. Liu, Y. Tang, Q. Xu, Y. Cao, J. Wei, Z. Liang, X. Jiang, Y. Wu, C. Guo, *J. Luminescence* **2024**, *271*, 120583.
[8] M. W. Alam, P. Saravanan, M. Selvaraj, P. Rosaiah, G. P. Nunna, T. J. Ko, *Waste Biomass Valorizat.* **2025**, *16*, 3295.
[9] N. K. B. Lotey, R. Lemos, F. D Silva, A. Deshmukh, N. Singh, S. Wankhede, R. Davuluri, N. Vishe, S. Kulkarni, *J. Fluoresc.* **2025**.
[10] Q. Wang, Z. Tang, L. Li, J. Guo, L. Jin, J. Lu, P. Huang, S. Zhang, L. Jiao, *Spectrochim. Acta, Part A* **2022**, *280*, 121538.
[11] Y. Han, Y. Liu, H. Zhao, A. Vomiero, R. Li, *J. Mater. Chem. B* **2021**, *9*, 4111.
[12] J.-R. Macairan, D. B. Jaunky, A. Piekny, R. Naccache, *Nanoscale Adv.* **2019**, *1*, 105.
[13] N. Navya, B. R. R. Krushna, S. C. Sharma, A. R. Srinivasan, A. George, S. Sunder mohapatra, C. Krithika, A. Bhanu, K. Manjunatha, S. Y. Wu, H. Nagabhushana, *Mater. Today Sustain.* **2024**, *27*, 100840.
[14] Y. Li, X. Xiao, Z. Wei, Y. Chen, *Zeitschrift für anorganische und allgemeine Chemie* **2022**, *648*, 202100323.
[15] K. R. M. Da Silva, C. M. S. Calado, T. V. Dos Santos, T. de Oliveira Sales, R. da Silva Viana, U. Rocha Silva, R. A. S. Ferreira, L. D. Carlos, C. D. A. E. S-Barbosa, *J. Mater. Chem. C* **2022**, *10*, 11614.
[16] F. Lin, M. Jia, Z. Sun, Z. Fu, *Scr. Mater.* **2020**, *186*, 298.
[17] R. Li, X. Wu, Y. Chen, Q. Zeng, T. Deng, T. Yu, *ACS Appl. Nano Mater.* **2024**, *7*, 15288.
[18] B. Zheng, J. Fan, B. Chen, X. Qin, J. Wang, F. Wang, R. Deng, X. Liu, *Chem. Rev.* **2022**, *122*, 5519.
[19] M. Quintanilla, L. M. Liz-Marzán, *Nano Today* **2018**, *19*, 126.
[20] Y. Wang, R. Yang, Y. Zhao, L. Hong, S. Ye, *Adv. Opt. Mater.* **2024**, *12*, 2302485.
[21] L. Zhang, Y. Ji, W. Li, B. Zhang, Q. Ma, B. Qin, Y. Zhang, D. Yue, Z. Wang, *Ceram. Int.* **2024**, *50*, 28967.
[22] M. Sun, L. Zhang, S. Xu, B. Yu, Y. Wang, L. Zhang, W. Zhang, *Analyst* **2022**, *147*, 947.
[23] Q. Zhong, T. Chen, M. Zhang, X. Chen, *Microchem. J.* **2024**, *206*, 111598.
[24] X. Xu, W. Li, W. Zhou, G. Tan, Y. Zheng, C. Hu, B. Lei, X. Zhang, Y. Liu, J. Zhuang, *J. Mater. Chem. C* **2018**, *6*, 10360.
[25] J. J. Carvajal Martí, (Ed. M. C. Pujol Baiges), in *Luminescent Thermometry: Applications and Uses*, Springer International Publishing, Cham **2023**.
[26] Y. Zhou, D. Zhang, J. Zeng, N. Gan, J. Cuan, *Talanta* **2018**, *181*, 410.
[27] S. Wang, J. Jiang, Y. Lu, J. Liu, X. Han, D. Zhao, C. Li, *J. Lumin.* **2020**, *226*, 117418.

[28] S. Yan, D. Pi, Y. Zi, H. Zhao, R. Feng, K. Ruan, J. Qiu, Z. Song, A. Huang, Y. Liu, Y. Cun, Z. Yang, *J. Mater. Chem. C* **2024**, *12*, 9606.
[29] D. J. Jovanović, Ž. Antić, R. M. Krsmanović, M. Mitric, V. Dordevic, B. Bartova, M. D. Dramicanin, *Opt. Mater.* **2013**, *35*, 1797.
[30] D. Gong, K. M. Holtman, D. Franqui-Espiet, W. J. Orts, R. Zhao, *Biomass Bioenergy* **2011**, *35*, 4435.
[31] Z. Tian, J. Chen, X. Ji, Q. Wang, G. Yang, P. Fatehi, *BioResources* **2017**, *12*, 2609.
[32] A. Corti, E. Torrens, D. Montané, *Biomass Convers. Biorefinery* **2023**, *13*, 2729.
[33] M. J. Antal, T. Leesomboon, W. S. Mok, G. N. Richards, *Carbohydrate Res.* **1991**, *217*, 71.
[34] J. Poerschmann, B. Weiner, R. Koehler, F.-D. Kopinke, *ACS Sustainable Chem. Eng.* **2017**, *5*, 6420.
[35] T. Gagic, A. Perva-Uzunalic, Z. Knez, M. Skerget, *J. Serb. Chem. Soc.* **2020**, *85*, 97.
[36] X. Kang, Y.-Y. Wang, S. Wang, X. Song, *Carbohydr. Polym.* **2021**, *255*, 117391.
[37] L. Almhofer, R. H. Bischof, M. Madera, C. Paulik, *Canad. J. Chem. Eng.* **2023**, *101*, 2033.
[38] R. Hiesgen, J. Haiber, in *Structural Properties: Atomic Force Microscopy In Encyclopedia of Electrochemical Power Sources*, Elsevier, Amsterdam, Netherlands **2009**.
[39] H. Ding, S.-B. Yu, J.-S. Wei, H.-M. Xiong, *ACS Nano* **2016**, *10*, 484.
[40] R. Ludmerczki, S. Mura, C. M. Carbonaro, I. M. Mandity, M. Carraro, N. Senes, S. Garroni, G. Granozzi, L. Calvillo, S. Marras, L. Malfatti, P. Innocenzi, *Chem. - Eur. J.* **2019**, *25*, 11963.
[41] F. Rigodanza, M. Burian, F. Arcudi, L. Đorđević, H. Amenitsch, M. Prato, *Nat. Commun.* **2021**, *12*, 2640.
[42] R. Xie, L. Zhang, H. Xu, Y. Zhong, X. Sui, Z. Mao, *Chem. Eng. J.* **2017**, *310*, 79.
[43] S. P. Ratnayake, M. M. M. G. P. G. Mantilaka, C. Sandaruwan, D. Dahanayake, R. Murugan, S. Kumar, G. A. J. Amaratunga, K. M. Nalid de Silva, *Appl. Catal. A: General* **2019**, *570*, 23.
[44] Z. Shu, M. Du, M. Li, Y. Liu, L. Gan, X. Zhang, W. Gui, *Luminescence* **2023**, *38*, 1521.
[45] T. Xiao, Y. Li, T. Wang, Y. Fan, F. He, O. Wang, J. Han, Z. Yin, Z. Yang, J. Qiu, Z. Song, *Mater. Chem. Front.* **2021**, *5*, 4280.
[46] S. Mondal, D. Khastgir, *Compos.: Part A* **2017**, *102*, 154.
[47] B. Van Dam, H. Nie, B. Ju, E. Marino, J. M. J. Paulusse, P. Schall, M. Li, K. Dohnalova, *Small* **2017**, *13*, 1702098.
[48] Y. Liu, G. Liu, J. Wang, X. Dong, W. Yu, *New J. Chem.* **2015**, *39*, 8282.
[49] S. Han, Y. Du, J. Yuan, Y. Tao, Y. Wang, S. Yan, D. Chen, *J. Non-Cryst. Solids* **2020**, *532*, 119894.
[50] F. He, P. Yang, D. Wang, N. Niu, S. Gai, X. Li, M. Zhang, *Dalton Trans.* **2011**, *40*, 11023.
[51] T. Samanta, A. E. Praveen, V. Mahalingam, *J. Mater. Chem. C* **2018**, *6*, 4878.
[52] T. O. Sales, R. J. Amjad, C. Jacinto, M. R. Dousti, *J. Lumin.* **2019**, *205*, 282.
[53] S. Wang, B. Sun, Z. Su, G. Hong, X. Li, Y. Liu, Q. Pan, J. Sun, *Inorg. Chem. Front.* **2022**, *9*, 3259.
[54] J. Y. Jung, J. Y. Park, W. T. Hong, Y. K. Kim, H. K. Yang, *Ceram. Int.* **2024**, *50*, 7908.
[55] S. Yang, H. Zhang, K. Jian, L. Fu, D. Lan, X. Zhao, *Chem. Eng. J.* **2024**, *500*, 157119.
[56] P. M. Olmos-Moya, E. Móntes, L. V. Ramírez, J. M. Sánchez, L. Álvarez-Valtierra, C. G. Solís, C. E. Molina Guerrero, M. A. Alpuche-Avilés, C. Pineda-Arellano, *J. Environ. Chem. Eng.* **2025**, *13*, 116226.
[57] A. Bezrukov, A. Galeeva, A. Krupin, Y. Galyametdinov, *Int. J. Mol. Sci.* **2024**, *25*, 5520.
[58] L. J. Mohammed, K. M. Omer, *Nanoscale Res. Lett.* **2020**, *15*, 182.
[59] X. Li, Y. Bao, X. Dong, L. Shi, S. Shuang, *Methods* **2021**, *13*, 4246.
[60] X. Long, J. Hu, H. Liu, S. Wu, *ACS Appl. Nano Mater.* **2024**, *7*, 23434.
[61] L. J. Mohammed, K. M. Omer, *Sci. Rep.* **2020**, *10*, 3028.
[62] J. Zhu, H. Chu, J. Shen, C. Wang, Y. Wei, *J. Colloid Interface Sci.* **2021**, *586*, 683.
[63] Z. Guo, J. Luo, Z. Zhu, Z. Sun, X. Zhang, Z. C. Wu, F. Mo, A. Guo, *Dyes Pigments* **2020**, *173*, 107952.
[64] M. Garvas, S. Acosta, I. Urbančič, T. Koklic, J. Strancar, L. A. O. Nunes, P. Guttmann, P. Umek, C. Bittencourt, *Nano Select* **2021**, *2*, 1208.
[65] Y. Yang, Y. Wang, Y. Feng, X. Song, C. Cao, G. Zhang, W. Liu, *Talanta* **2020**, *208*, 120354.
[66] I. E. Kolesnikov, D. V. Mamonova, M. A. Kurochkin, V. A. Medvedev, E. Y. Kolesnikov, *Ceramics Int.* **2023**, *49*, 20699.
[67] K. Trejgis, K. Ledwa, A. Bednarkiewicz, L. Marciniak, *J. Alloys Compd.* **2022**, *898*, 162839.
[68] I. E. Kolesnikov, M. A. Kurochkin, E. V. Golyeva, D. V. Mamonova, A. A. Kalinichev, E. Y. Kolesnikov, E. Lahderanta, *Phys. Chem. Chem. Phys.* **2020**, *22*, 28183.
[69] S. A. Pfeiffer, S. Nagl, *Anal. Chem.* **2017**, *89*, 9400.
[70] L. Laysandra, D. Kurniawan, C.-L. Wang, W.-H. Chiang, Y.-C. Chiu, *ACS Appl. Mater. Interfaces* **2021**, *13*, 60413.
[71] Q. Zhu, Y. Sun, Y. Wang, Z. Xia, *Laser Photon. Rev.* **2025**, *19*, 2402225.
[72] E. Song, M. Chen, Z. Chen, Y. Zhou, W. Zhou, H. T. Sun, X. Yang, J. Gan, S. Ye, Q. Zhang, *Nat. Commun.* **2022**, *13*, 2166.